2

Large scale kinematics and dynamical modelling of the Milky Way nuclear star cluster

Within the central 10 pc of our Galaxy lies a dense cluster of stars. This nuclear star cluster forms a distinct component of the Galaxy, and similar nuclear star clusters are found in most nearby spiral and elliptical galaxies. Studying the structure and kinematics of nuclear star clusters reveals the history of mass accretion and growth of galaxy nuclei and central massive black holes. Because the Milky Way nuclear star cluster is at a distance of only 8 kpc, we can spatially resolve the cluster on sub-parsec scales. This makes the Milky Way nuclear star cluster a reference object for understanding the formation of all nuclear star clusters.

We have used the near-infrared long-slit spectrograph ISAAC (VLT) in a drift-scan to construct an integral-field spectroscopic map of the central ~9.5 pc × 8 pc of our Galaxy, and six smaller fields out to 19 pc along the Galactic plane. We use this spectroscopic data set to extract stellar kinematics both of individual stars and from the unresolved integrated light spectrum. We present a velocity and dispersion map from the integrated light spectra and model these kinematics using Kinemetry and axisymmetric Jeans models. We also measure radial velocities and CO bandhead strengths of 1 375 spectra from individual stars.

We find kinematic complexity in the nuclear star cluster's radial velocity map including a misalignment of the kinematic position angle by 9° counterclockwise relative to the Galactic plane, and indications for a rotating substructure perpendicular to the Galactic plane at a radius of 20″ or ~0.8 pc. We determine the mass of the nuclear star cluster within $r = 4.2$ pc to $(1.4^{+0.6}_{-0.7}) \times 10^7\ M_\odot$. We also show that our kinematic data results in a significant underestimation of the supermassive black hole (SMBH) mass.

The kinematic substructure and position angle misalignment may hint at distinct accretion events. This indicates that the Milky Way nuclear star cluster grew at least partly by the mergers of massive star clusters. Compared to other nuclear star clusters, the Milky Way nuclear star cluster is on the compact side of the $r_{\rm eff} - M_{\rm NSC}$ relation. The underestimation of the SMBH mass might be caused by the kinematic misalignment and a stellar population gradient. But it is also possible that there is a bias in SMBH mass measurements obtained with integrated light, and this might affect SMBH mass determinations of other galaxies.

A. Feldmeier, N. Neumayer, A. Seth, R. Schödel, N. Lützgendorf, P. T. de Zeeuw, M. Kissler-Patig, S. Nishiyama, C. J. Walcher

Astronomy & Astrophysics, Volume 570, id.A2, 20 pp, 10/2014

2.1 Introduction

The Milky Way nuclear star cluster lies within the central 10 pc of our Galaxy and is composed of a dense population of stars. The cluster forms a distinct component, with a half-light radius or effective radius $r_{\rm eff}$ of $\sim$110−127″ (4.2−5 pc, Schödel et al. 2014a; Fritz et al. 2016), and a mass of $(2-3)\times10^7\ M_\odot$ (Launhardt et al. 2002; Schödel et al. 2014a). However, the formation and growth of the nuclear star cluster and the supermassive black hole (SMBH) in the centre are not understood. The stars in the cluster provide a record of the nuclear accretion history and formation processes.

The nuclear star cluster in the Galactic centre is not a unique object, as such clusters are common in other galaxies as well. They have been detected in ∼75 per cent of spiral galaxies (Carollo et al. 1998; Böker et al. 2002), and spheroidal galaxies (Côté et al. 2006). These are lower limits, as the presence of bulges and dust lanes can obscure the nuclear cluster and prevent detection (Carollo et al. 2002; Seth et al. 2006). Galaxies with higher mass than $\sim10^{10}\ M_\odot$ usually only host a SMBH, while nuclear star clusters are preferentially detected in galaxies with lower mass (Ferrarese et al. 2006; Wehner & Harris 2006; Böker 2010; Scott & Graham 2013). But there are also cases where both nuclear star cluster and SMBH coexist in the same galactic nucleus (Seth et al. 2008a). The most convincing case is our own Galaxy. Precise measurements of stellar orbits around the central radio source Sagittarius A* (Sgr A*) provide the most direct evidence for the presence of a SMBH at the centre of our Galaxy. Ghez et al. (2008) and Gillessen et al. (2009b) observed a full Keplerian orbit of one of the innermost stars and measured the mass of the black hole as $\sim4\times10^6\ M_\odot$. Also other nuclear clusters show evidence for a central massive black hole from dynamical modelling or the presence of an AGN (e.g. Filippenko & Ho 2003; Graham & Spitler 2009; Seth et al. 2010; Neumayer & Walcher 2012).

With a distance of only ∼8 kpc (Ghez et al. 2008; Gillessen et al. 2009b) it is possible to resolve single stars in the Milky Way nuclear star cluster spectroscopically and infer their age. The stellar populations of the central 1 pc (∼ 26″) of the Milky Way can be studied only in the near-infrared (e.g by Pfuhl et al. 2011; Do et al. 2013a), as high extinction makes the Galactic centre impenetrable for observations in the visible bands. The stars are predominantly cool and old (> 5 Gyr old, e.g. Blum et al. 2003; Pfuhl et al. 2011), but in the central ∼0.5 pc there exists an additional stellar component in the form of hot, young stars (4 − 8 Myr e.g. Paumard et al. 2006; Lu et al. 2009; Bartko et al. 2009), and stars of intermediate age (∼100 Myr, e.g. Krabbe et al. 1995; Pfuhl et al. 2011). So far, multiple stellar populations have been found in all other nuclear star clusters as well (e.g. Walcher et al. 2006; Rossa et al. 2006; Seth et al. 2006; Siegel et al. 2007; Seth et al. 2010; Lauer et al. 2012), with an underlying old population (> 1 Gyr) and a generation of younger stars (< 100 Myr). This suggests a complex star formation history.

There are two prevalent formation scenarios for nuclear star clusters: 1) Stars form in dense clusters elsewhere in the galaxy and then migrate to the galaxy's centre. Tremaine et al. (1975) suggested the formation of the M31 nucleus by the infall of globular clusters due to dynamical friction. The clusters would merge to become the observed nuclear star cluster.

Capuzzo-Dolcetta & Miocchi (2008), Antonini (2013), Gnedin et al. (2014), and Antonini (2014) studied the infall of massive clusters in central regions of galaxies and found that the expected density and velocity-dispersion profiles of the merged nuclear star cluster matches the observations. 2) Nuclear star clusters form in-situ by gas infall from the disc followed by star formation (Milosavljević 2004; Pflamm-Altenburg & Kroupa 2009). This theory is supported by the discovery of rotation in the nuclear star clusters of the Milky Way (Trippe et al. 2008; Schödel et al. 2009) and NGC 4244 (Seth et al. 2008b). A combination of both formation scenarios is also possible (Hartmann et al. 2011; Neumayer et al. 2011; Turner et al. 2012; De Lorenzi et al. 2013).

At the Galactic centre the presence of young stars indicates star formation within the past few Myr, as well as the presence of molecular gas within a few pc of Sgr A*. This demonstrates that the necessary material for star formation can be found within the nuclear star cluster. The ring of clumpy gas and dust is called circumnuclear disc or circumnuclear ring and extends to a Galactocentric radius of ∼7 pc (3′, e.g. Yusef-Zadeh et al. 2001; Christopher et al. 2005; Lee et al. 2008; Liu et al. 2012). Oka et al. (2011) suggested that the circumnuclear disc was formed from an infalling disrupted giant molecular cloud, and may eventually fragment and trigger star formation. Yusef-Zadeh et al. (2008) detected methanol masers, which could hint to an early stage of star formation.

There are several kinematic studies of the stars in the central parsec of the Milky Way nuclear star cluster. For example Trippe et al. (2008) and Schödel et al. (2009) studied both radial velocities and proper motions but not beyond a distance of 1 pc from the Galactic centre. They found that the velocity dispersions of the stars are consistent with an isotropic, rotating cluster. However, the larger-scale kinematics are not so extensively studied. Lindqvist et al. (1992b) collected a sample of 134 OH/IR stars at a distance of 5−100 pc (∼2−40′) from the Galactic centre, but only 15 of their targets are within 8 pc from the Galactic centre, and therefore likely cluster members. McGinn et al. (1989) obtained integrated light spectra of selected fields with a 20″ (0.78 pc) aperture at 2.3 μm out to ∼4 pc (1.′7) distance along the Galactic plane and ∼1.5 pc (0.′6) perpendicular to it. They found decreasing velocity dispersion and increasing velocities with Galactocentric distance, and a flattening of the rotation curve between 2 pc and 3 pc (∼50 − 80″). But McGinn et al. (1989) had large scattering in their data.

Hence the Milky Way nuclear star cluster kinematics are known in detail at small scales, but the large scale kinematics beyond 1 pc remain uncertain. For example, the rotation is not yet well determined, although a rotation law can provide insights on the processes that play a role in the formation of the nuclear star cluster. Calculations of the Galactic potential beyond 1 pc used $\lesssim$200 stars to trace the kinematics, but the stars were spread over a large area of several tens of pc^2. Therefore there is large uncertainty in these measurements.

In order to overcome this lack of knowledge we have obtained a new spectroscopic data set of the Milky Way nuclear star cluster on a large scale, covering the central ∼9.5 pc × 8 pc (4′ × 3.′5). The purpose of this work is two-fold: (i) to perform the first detailed kinematic analysis of the Milky Way nuclear star cluster on large scales in integrated light; (ii) to construct a dynamical model, in which we derive the cluster mass and constrain the central

Galactic potential. As by-product we also extract an H_2 gas kinematic map and almost 1 400 spectra of bright stars. We compute the velocities and CO indices of these stars, from which we can identify young star candidates.

This paper is organised as follows: The observations are summarised in Section 2.2, and in Section 2.3 we describe the data reduction and analysis. Our results for the stellar kinematics and stellar populations are presented in Section 2.4. In Section 2.5 we fit a surface brightness profile and present the results of dynamical Jeans models. We discuss our results in Section 2.6. Our conclusions are provided in Section 2.7. The H_2 gas emission line results are shown in Appendix 2.9. Throughout this paper we assume a Galactocentric distance R_0 of 8.0 kpc (Malkin 2012), i.e. $1''$ corresponds to ∼0.039 pc.

2.2 Observations

We used the near-infrared long-slit spectrograph ISAAC (Infrared Spectrometer And Array Camera, Moorwood et al. 1998) in a drift-scan technique to observe the central ∼9.5 pc × 8 pc ($4' \times 3\farcm5$) of our Galaxy. To complement our data set we also observed six fields out to a distance of ∼19 pc ($8'$) along the Galactic plane, a region where the nuclear stellar disc becomes important.

Observations were performed on VLT-UT3 (Melipal) in the nights of July 3 and 4, 2012. We used the ISAAC short wavelength medium resolution spectroscopic mode. In this mode the spectral coverage is only 0.122 μm. The central wavelength of our observations is 2.35 μm, and the resulting spectral range is ∼2.289 − 2.411 μm. The ISAAC slit has a length of $120''$, and we chose a slit width of $0\farcs6$ to obtain a spectral resolution of $R = 4\,400$, corresponding to $\Delta V \approx 68\,\mathrm{km{\cdot}s^{-1}}$. The spatial pixel scale is $0\farcs148{\cdot}\mathrm{pixel}^{-1}$, the spectral pixel size is $1.2 \times 10^{-4}\,\mu\mathrm{m{\cdot}pixel^{-1}}$. The drift scan worked as follows: To cover the Galactic nuclear star cluster to the effective radius, we scanned the slit across the Galactic centre while integrating. During every 120 s exposure, the slit moved perpendicular to the slit length over $2''$. The scan direction was along the Galactic plane applying a position angle of $31\fdg40$ east of north (J2000.0 coordinates, Reid & Brunthaler 2004). During the first night we scanned the central $\sim 120'' \times 240''$. In the second night we scanned a smaller region north-west of the centre, which partly overlaps with the observations of the first night, covering $\sim 120'' \times 120''$. Additionally we observed six smaller regions with $\sim 120'' \times 16''$ each along the Galactic plane. They are at distances from the centre of $4'$, $6'$, and $8'$, respectively. The scanned regions are illustrated in Fig. 2.1.

For sky observations we made offsets to a dark cloud that is located about $30'$ east of the Galactic Centre ($\alpha \approx 267\fdg00$, $\delta \approx -28\fdg99$, diameter approximately $11'$, Dutra & Bica 2001). The sky was also observed in a drift scan with the same scanning velocity. After a sequence of 8 − 10 object frames we made sky offsets and followed an object − sky − object sequence. We obtained five spectroscopic sky exposures in each sky offset, in order to remove stars in the sky field and compute a Mastersky frame. Moreover, we observed four B dwarfs as telluric

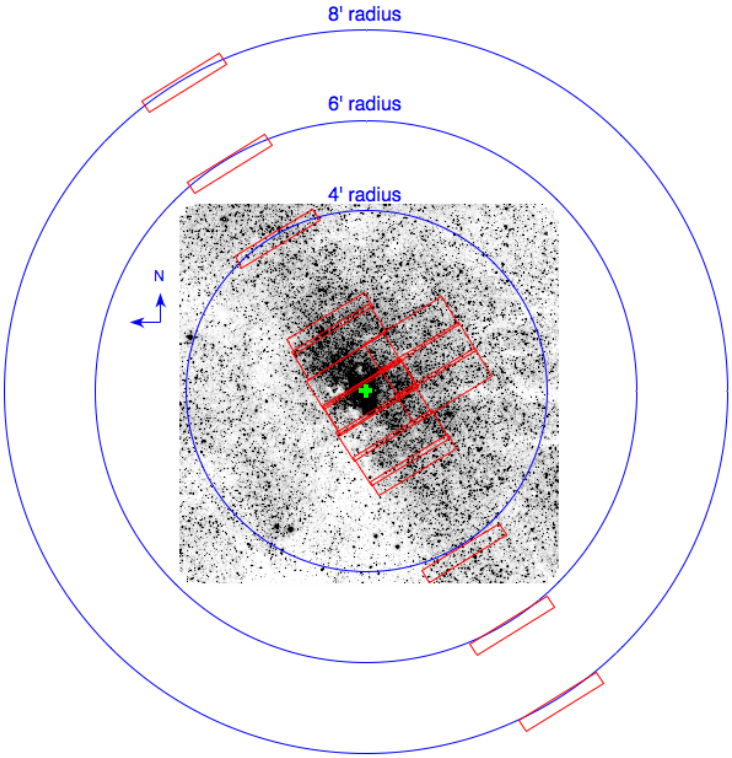

Figure 2.1: Positions of the regions scanned with ISAAC (red rectangles). The underlying image is from IRSF/SIRIUS in K_S band (Nishiyama et al. 2006). The circles denote a distance of 4′, 6′, and 8′ from the position of Sgr A*, respectively, and the green cross is the position of Sgr A*. The outer fields are not exactly symmetric due to the drift towards the south-west during the acquisition.

standards in both nights using a standard nodding technique. For wavelength calibrations we obtained Xenon and Argon arc lamp calibration frames.

2.3 Data reduction and analysis

2.3.1 Data reduction

The data reduction of the spectra included the following steps: First we used the ISAAC pipeline ISAACP (Amico et al. 2002) to remove electrical ghosts from all frames with the recipe GHOST, and with the recipe SP_FLAT we obtained master flats. We further combined the dark files to master darks and subtracted them using IRAF (Imaging Reduction and Analysis

Facility[1]), and removed bad pixels. For cosmic ray removal we used the LAPLACIAN COSMIC RAY IDENTIFICATION L.A.COSMIC written by van Dokkum (2001). Flat fielding as well as distortion correction and wavelength calibrations were performed with IRAF. The spectra contain thermal background, which is partly due to the sky and partly to the detector. We made a robust two-dimensional polynomial fit to each two-dimensional spectral frame along the dispersion axis and subtracted the polynomial fit from the spectra.

Unfortunately, the spectra suffer from persistence. This means that bright stars, especially those which were saturated in the images taken before the spectra, were burnt in the detector and remain visible for some time as bright spots in the spectra taken afterwards. Our approach to remove the persistence from the spectra is described in Appendix 2.8. After subtracting the persistence from object and sky spectra we combined the sky frames to master sky frames and performed sky subtraction with an IDL routine written by Davies (2007).

We reduced the telluric spectra using the double sky subtraction technique, which is the standard for nodding, to ensure optimal sky subtraction. A telluric correction was performed for every single row of the two-dimensional spectral frames separately with the IRAF task TELLURIC. We scaled the intensity of the telluric spectra with the difference in air mass and searched for an optimum scale factor, but omited a shift option for the telluric correction. The next step was to shift the reduced spectra to the local standard of rest using the IRAF recipes RVCORRECT and DOPCOR.

To determine the astrometry of our spectra, we created images from spectra taken subsequently before a sky offset. We summed the flux of every spectrum along the dispersion axis and reconstructed images, where every exposure extends over 15 columns of the ISAAC pixel scale of $0\farcs148 \cdot \mathrm{pixel}^{-1}$. This means we have a spatial resolution of $2\farcs22$ in the drift direction (Galactic east-west) and a spatial resolution of $0\farcs148 \cdot \mathrm{pixel}^{-1}$ along the slit (Galactic north-south direction). Every red box in Fig. 2.1 corresponds to one reconstructed image. The image was blurred with a Gaussian point spread function (PSF) with the full width half maximum (FWHM) of the seeing during the observations. This makes the stars less rectangular. The images were cross correlated with the ISAAC acquisition images that were matched to the 2MASS point source catalogue (Skrutskie et al. 2006) and also blurred. While the wavelength range of the acquisition images covers the entire K-band, the spectra contain a much narrower wavelength range. Still, we could identify enough stars to perform a meaningful cross correlation. Thus we obtained the astrometry for every spectrum.

We compared the reconstructed image in the new coordinate system with stars from star catalogues (2MASS point source catalogue by Skrutskie et al. 2006, and the star catalogue constructed by Nishiyama et al. 2006). Thereby we found a systematic distortion along the slit direction by up to 6 pixels. We measured the positions of bright stars along the slit and computed the offset from the expected position as in the star catalogue. This deviation was modelled by a second order polynomial, and the data was resampled along the slit direction. After applying the distortion correction to all spectra, the mean offset of the position of bright

[1]IRAF is distributed by the National Optical Astronomy Observatory, which is operated by the Association of Universities for Research in Astronomy (AURA) under cooperative agreement with the National Science Foundation.

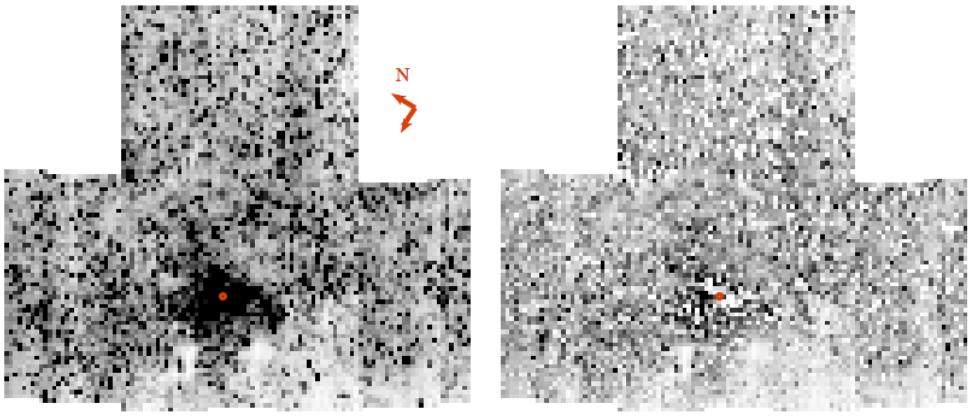

Figure 2.2: Reconstructed data cube from all central exposures, covering ~240″× 210″, flux summed over 2.29 − 2.365 μm. The left panel uses all available data, i.e. the full data cube. The right panel is the data cube after removing foreground and background stars based on their colour, and stars brighter than K_S =11.5 mag, i.e. the cleaned data cube. It contains only light from faint member stars. The red point denotes Sgr A*. The maps are oriented with the Galactic plane horizontally and Galactic North up and Galactic East left. The arrows indicate the orientation in the equatorial system. Both images are in the same linear flux scaling.

stars along the slit to the position of the star catalogue was reduced from 0.9 to 0.2 pixels, and we reran the cross correlation.

We could identify single bright stars in the unbinned data using the aforementioned catalogues. We selected all stars brighter than $K_S = 11.5$ mag within our observations and extracted their spectra. These stars are much brighter than the sun and thus mostly RGB and AGB stars. For comparison, a solar mass star has a K-band magnitude of 20 − 21 mag at a distance of 8 kpc with an extinction of $A_{K_S} = 2 - 3$ mag. The position of the star along the slit and its FWHM were fitted with a Gaussian function. We extracted the spectrum within two times the FWHM[2]. The median signal-to-noise ratio (S/N) for these spectra is 25, which is high enough to fit the kinematics.

To examine also the contribution of the fainter stars we constructed a single data cube by combining the spectra of the central field in the form of a "T", which is roughly 240″×210″ (see Figs. 2.1 and 2.2). We determined a relative flux calibration factor for every sequence of subsequently taken spectra before putting the data set of the central field together. To calibrate the relative flux we used an IRSF/SIRIUS image in K_S-band (Nishiyama et al. 2006), and the reconstructed images with the flux between 2.29 and 2.365 μm summed up. We estimate the uncertainty for the relative flux calibration to be about 10 per cent.

To bin the data to one data cube, we summed up 15 ISAAC pixel rows along the slit, multiplied with the respective flux calibration factor, and obtained a final pixel size of 2.″22 × 2.″22. The cube extends over ~240″ along the Galactic plane and ~210″ in perpendicular

[2]These spectra are publicly available at the CDS.

direction. We used our ISAAC data to produce two separate data cubes: 1) A data cube with the full integrated light in each $2\farcs22 \times 2\farcs22$ pixel[3]. 2) A data cube with the brightest stars, foreground, and background stars removed. We will refer to these products as "full data cube" and "cleaned data cube". The full data cube, integrated in wavelength direction, is shown on the left panel in Fig. 2.2. For the very centre we have multiple exposures, which were combined by taking the arithmetic mean. We also constructed a noise cube, containing the uncertainty of the persistence removal and sky subtraction.

To produce the cleaned data cube, we cut out stars from the unbinned data before setting up the $\sim 240'' \times 210''$ data cube. By cutting out the brightest stars ($K_S \leq 11.5$ mag, i.e. $K_{\rm cut} = 11.5$ mag), we obtained light just from the underlying fainter population, reducing the effects of shot noise caused by single stars in our data cube. In addition to removing the brightest stars, we also used colour information to remove the fainter foreground and background stars. For this purpose we applied colour cuts and assumed that all stars with $H-K_S < 1.5$ mag or $H-K_S > 3.5$ mag are foreground or background stars, respectively. Our exclusion criterion is more inclusive than the one applied by Schödel et al. (2010), who excluded all stars with $H-K_S < 1.8$ mag or $H-K_S > 2.8$ mag. We removed foreground and background stars brighter than magnitude $K_S = 14$ mag. For stars fainter than $K_S = 14$ mag we cannot reliably determine their position along the slit and might misidentify a cluster member star. After fitting the position and FWHM of a star which we want to cut out, we set the pixel counts within one FWHM on either side of the position of the star to zero. The integrated light of the cleaned data cube is shown in Fig. 2.2 (right panel). Some of the pixels are empty and hence contain no information at all.

2.3.2 Deriving stellar kinematics

To derive stellar kinematics we fitted the line-of-sight-velocity distribution (LOSVD) of the CO absorption lines ($2.2902 - 2.365\,\mu$m). These lines are most prominent in cool late-type stars with several Gyr age. Moreover, the CO lines are an excellent tracer of the stellar kinematics in the highly extinction affected Galactic centre region because the CO lines lie within the near-infrared K-band, where extinction is low enough to allow for sensitive observations. To obtain the LOSVD, we used the IDL routine pPXF (Cappellari & Emsellem 2004). It recovers the Gauss-Hermite parameters $(V, \sigma, h_3, h_4, ...)$ of the LOSVD by convolving template spectra with the parameterised LOSVD and finding the best fit to the observed spectrum in pixel space. We fitted only the first two moments of the LOSVD, the first moment corresponds to the velocity, the second moment to the velocity dispersion. As template spectra we used the high-resolution ($R \geq 45\,000$) spectra of Wallace & Hinkle (1996), which contain supergiant, giant, and dwarf star spectra in the spectral types from G to M. Those spectra were convolved with a Gaussian to obtain the same spectral resolution as our data set. The program pPXF finds an optimal template, which is a linear combination of the template spectra. The optimal template convolved with the LOSVD recovers the shape of the integrated light spectrum. Errors were calculated from Monte Carlo simulations. We added random

[3]This data cube is publicly available at the CDS.

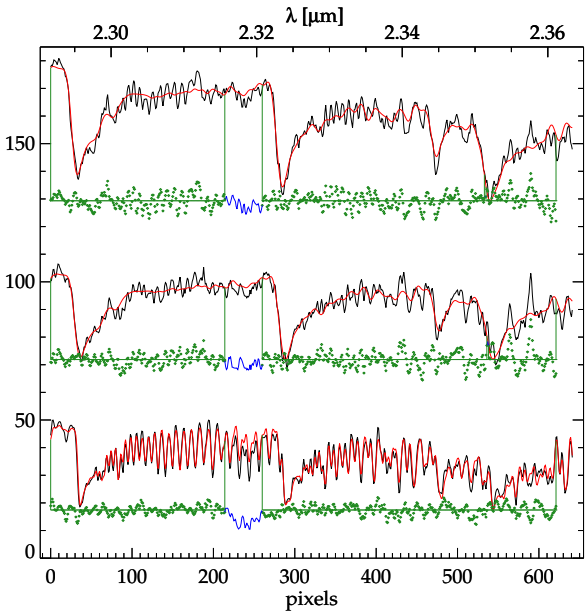

Figure 2.3: Example of CO absorption line spectra (black) of a Voronoi bin of the full data cube (upper spectrum), a Voronoi bin of the cleaned data cube (middle spectrum) and of a single star (lower spectrum). The red lines are the pPXF-fits to the data. The blue regions are not fitted, as there is a strong telluric absorption line in this wavelength region. Green dots are the residuals of the fits. The fluxes of the spectra are scaled for this plot.

noise to the spectra in each pixel and calculated the LOSVD in 100 runs. The fits were performed in the wavelength range of $2.2902 - 2.365\,\mu$m, which contains four CO absorption lines, ^{12}CO (2-0), ^{12}CO (3-1), ^{13}CO (2-0), and ^{12}CO (4-2).

We used the two data cubes to obtain a velocity and velocity dispersion map of the integrated light. By applying adaptive spatial binning (Cappellari & Copin 2003) to our data we make sure that the integrated spectrum of every bin has approximately the same signal-to-noise ratio (S/N). Therefore we calculated the S/N for every single pixel of the data cubes with pPXF before the binning. We then summed the spectra of all pixels in a Voronoi bin to one integrated light spectrum per bin and fitted the LOSVD. Figure 2.3 shows three example spectra, and the respective fits. The upper spectrum is an integrated light spectrum from the full data cube, the middle spectrum is from the cleaned data cube, and the lower spectrum is from a single bright star. Figure 2.4 shows the velocity and velocity dispersion maps for a binning of at least S/N = 60 for the full data cube. One can see the rotation of the nuclear star cluster around Sgr A*, and an increase of the velocity dispersion up to $\sim$200 km·s^{-1}. The bright supergiant star IRS 7 with apparent magnitude $K_S \approx 7.0$ mag (Schödel et al. 2013) dominates its bin, and the bin has therefore only low velocity dispersion. Figure 2.5 shows the kinematic maps for the data cube where single stars are cut out. It appears smoother and

less affected by shot noise. Some pixels contain no information at all after the bright stars and foreground stars were cut out, and those pixels are displayed in white.

To quantify the amount of shot noise in the cleaned data cube we produced two additional cleaned data cubes for which we vary the magnitude of the stars we cut out from $K_{\rm cut} = 11.5$ mag to $K_{\rm cut} = 11$ mag and $K_{\rm cut} = 12$ mag. On these data cubes we applied the same Voronoi binning as on the cleaned data cube. The number of stars per bin in the data cube with $K_{\rm cut} = 11$ mag increased by 1.85 on average, and decreased in the data cube with $K_{\rm cut} = 12$ mag by 2.3 on average. We find that a variation of the magnitude cut by 0.5 mag has no strong influence on our results. In 75 per cent of all Voronoi bins the difference of the velocity measurements by varying $K_{\rm cut}$ by 0.5 mag is less than the velocity uncertainties. For only 5 per cent of all Voronoi bins the difference is more than two times the velocity uncertainties. The difference of the velocity measurements has a standard deviation of $8.2\,{\rm km\cdot s^{-1}}$. There is also no systematic trend in the velocity dispersions obtained from the different cleaned data cubes. The difference of the velocity dispersions in the same bin from the different cleaned data cubes has a mean value of $0.7\,{\rm km\cdot s^{-1}}$. We conclude that on average our measurements are robust and not severely influenced by shot noise.

We further estimated the shot noise in the velocity map obtained from the full data cube by a comparison of the total flux in each Voronoi bin with the flux given by a K-band luminosity function (KLF). Therefore we used the surface brightness profile from Section 2.5.1 scaled to the K-band. We calculated the total flux for each Voronoi bin by multiplying the surface brightness at a given bin with the respective area covered by the bin. The KLF tells us how many stars of a given magnitude are present in the nuclear star cluster. We used the KLF of Zoccali et al. (2003, their Table 3), which was measured in the Galactic bulge. However, Genzel et al. (2003) showed that the KLF of the central $9''$ of the Milky Way nuclear star cluster is very similar to the KLF measured by Zoccali et al. (2003). For a rough estimation of the number of stars we can therefore assume that a normalised KLF does not vary strongly over the entire field. We computed the integrated flux of the normalised KLF. Therefore we considered the KLF only for stars brighter than $K_S = 17$ mag, since this is the approximate magnitude limit for red clump stars, and fainter stars have rather weak CO absorption features. A comparison with the total flux of the Voronoi bins tells us that in each bin we expect at the least 740 stars and 5 500 stars on average. When we assume that the brightest star in a Voronoi bin has a magnitude of $K_S = 7.27$ mag, the fraction of light it would contribute to a Voronoi bin is 12 per cent on average, and 51 per cent in the worst case. The high light fraction of single stars indicates that shot noise can have a severe effect on results obtained from the full data cube.

According to the KLF, the stars fainter than $K_S = 11.5$ mag contribute 36 per cent of the total flux of the nuclear star cluster. So, in the Voronoi bins of the cleaned data cube the total flux is decreased to 36 per cent. We compared the remaining flux of a Voronoi bin of the cleaned data cube with the flux of a star with $K = 11.52$ mag. We found that a single star of $K_S = 11.52$ mag contributes at maximum 1.9 per cent of the remaining light of the Voronoi bin. This is significantly decreased compared to the maximum light fraction of 51 per cent of the full data cube. Even if all the light of the cleaned data cube would come from the brightest

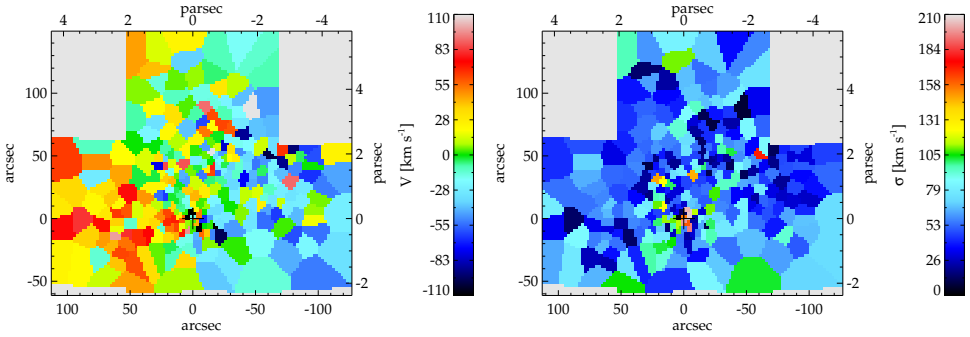

Figure 2.4: CO absorption line map of velocity, and velocity dispersion (left, and right, respectively) obtained by using the full data cube. Both, velocity and velocity dispersion are in units of km·s^{-1}. The coordinates are centred on Sgr A* and along the Galactic plane with a position angle of 31°.40. The plus sign marks the position of Sgr A*. The velocity is in the local standard of rest, Galactic North is up, Galactic East is left.

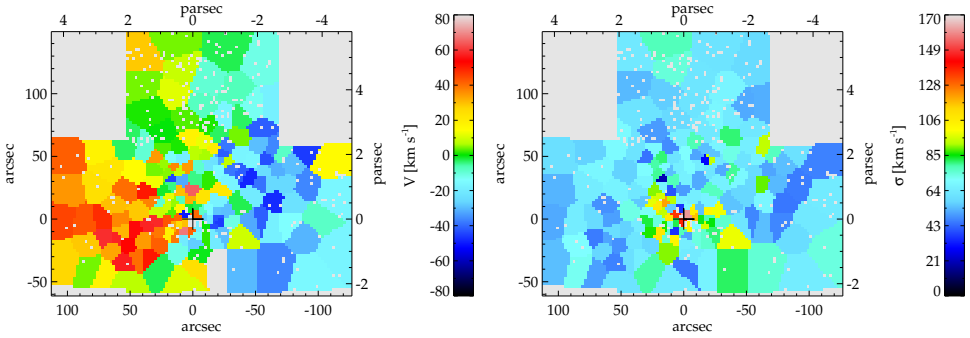

Figure 2.5: Same as Fig. 2.4, but for the cleaned data cube. White pixels mark regions where there was no signal left after cutting out stars.

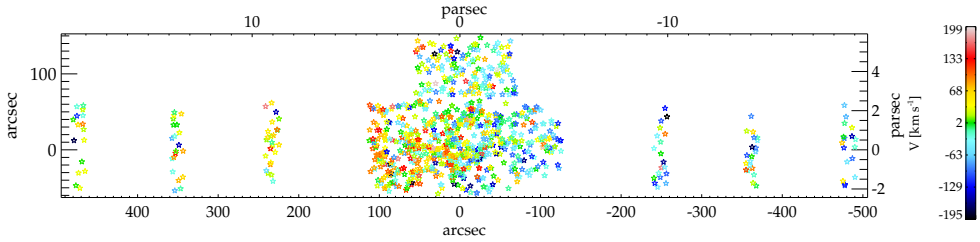

Figure 2.6: Velocity map of 1 094 bright stars ($K_S \leq 11.5$ mag) with CO absorption lines in the colour interval 1.5 mag $\leq H - K_S \leq$ 3.5 mag. We plot only stars with S/N > 12 and $|V| < 200$ km·s^{-1}.

stars with $K_S = 11.52$ mag, there would be on average 400 of these stars in each bin, and at the least 53 stars. This shows that the influence of a single star is significantly decreased in the cleaned data cube, and shot noise is no longer an issue.

We also fitted the LOSVD for each spectrum of the single bright stars with $K_S \leq 11.5$ mag. From these 1 375 spectra we found that ∼1 200 are from stars in the colour range 1.5 mag ≤ $H - K_S \leq 3.5$ mag, suggesting their membership to the nuclear star cluster. Some of the spectra are from the same star, since we had overlapping exposures. The result for ten of these stars is shown in Table 2.1, the full Table is publicly available together with the spectra at the CDS. Figure 2.6 displays the velocity map of stars in the colour interval 1.5 mag ≤ $H - K_S \leq 3.5$ mag. The mean velocity of our data set is consistent with zero, and the standard deviation is 74 km·s^{-1}. The most extreme radial velocities we obtain are -340.3 ± 59.5 km·s^{-1} on the blue side, and 291.9 ± 1.5 km·s^{-1} on the red side. We also see rotation in the same sense as the Galactic rotation.

To ensure the accuracy of our wavelength calibration and velocity determination, we compared our derived velocities to previous stellar velocity measurements. The cleanest comparison is for the bright supergiant IRS 7, where we find a velocity of -116 ± 1 km·s^{-1}, in excellent agreement with the value from Reid et al. (2007, -114 ± 3 km·s^{-1}). For other stars our low spatial resolution along the galactic plane creates possible issues with contamination in our data. Comparing stellar velocities derived from SiO masers by Deguchi et al. (2004), we find that four stars have $\Delta V \leq 6$ km·s^{-1} (stars with names 3-6, 3-16, 3-5.2 and 16-49 in Deguchi et al. 2004). Two other stars have a 30 km·s^{-1} and 60 km·s^{-1} offset in velocity (stars with names 3-885 and 3-57 in Deguchi et al. 2004). These larger offsets could result from intrinsic changes in the velocities in pulsing AGB stellar atmospheres (Habing & Olofsson 2004), but for star 3-885 a misidentification is also possible. Overall, it appears that our absolute velocities are accurate to within approximately 5 km·s^{-1}.

The large field of view results in the radial direction not being constant over the entire field and the proper motion of the sun with respect to the Galactic centre has to be taken into account. We tested the amplitude of this so-called perspective rotation using Equation 6 of van de Ven et al. (2006). Assuming that the sun moves with $v_x = 220$ km·s^{-1} in the Galactic plane (Chaisson & McMillan 1993) at a distance of 8 kpc from the centre, and with $v_y = 7$ km·s^{-1} towards the Galactic North, we find that this effect is negligible perpendicular to the Galactic plane. Along the Galactic plane the perspective rotation is $\lesssim 0.13$ km·s^{-1} for the central field. For the outermost fields at 8′ distance from the centre, it is 0.5 km·s^{-1}. This is less than the usual velocity uncertainty we obtain. Nevertheless, we corrected the velocities of the six outer fields shown in Fig. 2.6 for perspective rotation.

Table 2.1: Table of stars with coordinates RA and Dec, K_S - and H-band magnitude according to the source catalogue, measured line-of-sight velocity V, CO index CO_{mag} and signal-to-noise ratio S/N. We only reproduce 13 lines of this table here. A full table with the spectra is available in electronic form at the CDS.

ID	RA [°]	Dec [°]	K_S [mag]	H [mag]	source catalogue	V $\left[\mathrm{km \cdot s^{-1}}\right]$	CO_{mag}	S/N
1	266.44606	−28.99290	11.24	13.50	SIRIUS	86.7 ± 1.6	0.31	21.1
2	266.44566	−28.99287	9.73	11.28	2MASS	80.9 ± 1.5	0.45	18.9
3	266.44671	−28.99027	11.02	14.12	SIRIUS	26.3 ± 3.6	0.40	18.7
4	266.44510	−28.99095	10.54	12.13	2MASS	−55.5 ± 0.2	0.48	22.4
5	266.44680	−28.98703	10.82	12.28	2MASS	34.9 ± 2.5	0.39	22.9
6	266.44453	−28.98938	11.48	14.13	SIRIUS	−4.9 ± 1.2	0.26	22.9
7	266.44371	−28.99045	10.32	11.91	2MASS	77.4 ± 1.8	0.40	17.9
8	266.44243	−28.99068	11.33	13.71	SIRIUS	63.3 ± 0.3	0.39	21.9
9	266.44301	−28.98553	10.44	13.40	SIRIUS	93.0 ± 1.0	0.30	16.2
10	266.44122	−28.98636	9.34	11.21	2MASS	−38.9 ± 0.7	0.51	20.2
high velocity stars								
521	266.41859	−29.00958	8.66	11.06	SIRIUS	−340.3 ± 59.5 [a]	0.07	16.7
1042	266.37746	−28.99331	11.41	13.35	SIRIUS	291.9 ± 1.5	0.20	22.2
1056	266.39317	−29.01596	10.14	11.87	2MASS	−265.6 ± 0.5	0.11	45.2

Notes. [(a)] The high uncertainty is caused by the limited wavelength range. In this spectrum there is no continuum on the blue side of the CO absorption line. However, this star is known as IRS 9 and its velocity was measured by Zhu et al. (2008) to $-347.8\,\mathrm{km \cdot s^{-1}}$.

2.3.3 Line strength measurements

With our data set we can give a rough age estimation of bright stars. We use the fact that CO absorption lines are prominent in old stars, but not in young, hot stars. To quantify the depth of the CO line, we used the CO index CO_{mag} in a colour-like way as defined by Kleinmann & Hall (1986)

$$CO_{\mathrm{mag}} = -2.5 \log \frac{F_a}{F_c}, \tag{2.1}$$

where F_a is the mean flux at the first CO absorption line ($2.2931 - 2.2983\,\mu$m), and F_c is the mean flux at the continuum ($2.2885 - 2.2925\,\mu$m), corrected for radial velocity shifts. This is not the same continuum wavelength region as defined in Kleinmann & Hall (1986), which is at shorter wavelengths. As we are very limited in our spectral range, we had to modify the CO index definition. To calibrate our CO_{mag} with a temperature, we used the IRTF Spectral Library (Rayner et al. 2009). The metallicities of both the stars in the library and in the Milky Way nuclear star cluster are near-solar (Cunha et al. 2007; Pfuhl et al. 2011). We computed CO_{mag} for giants and supergiants, with the spectral class ranging from F0 to M6. Lang (1992) lists the temperature of stars depending on the spectral class and type. The relation between effective temperature T_{eff} and CO_{mag} is shown in Fig. 2.7. We found that for stars with a temperature $T_{\mathrm{eff}} > 4\,800$ K, the CO_{mag} is less than 0.09. Using Padova isochrones for solar metallicity stars with $M_K \leq -3$ mag (which corresponds to $K_S \leq 11.5$ mag in the Galactic centre), we found that stars hotter than 4 800 K are younger than approximately 300 Myr. Therefore we conclude that stars with $CO_{\mathrm{mag}} < 0.09$ are younger than 300 Myr. Also for higher values of CO_{mag}, the CO index correlates roughly with the age of the stars.

2.4 Stellar kinematics and population results

2.4.1 Kinematic structure and substructure of the nuclear star cluster

In this section we show that the overall rotation of the Milky Way nuclear star cluster is misaligned by $\sim 9^\circ \pm 3^\circ$ counterclockwise from the major axis of the galaxy at radii from 1 to 4 pc. Furthermore, we find evidence for one cold rotating substructure within the central parsec.

We modelled the stellar kinematics of the velocity maps using KINEMETRY, which was developed by Krajnović et al. (2006). KINEMETRY assumes that the velocity profile along an ellipse around the centre can be expressed by a simple cosine law. The IDL routine written by Krajnović et al. (2006) divides the velocity map into individual elliptical rings, which are described by harmonic terms. The best fitting ellipse depends on two parameters, the kinematic position angle $\mathrm{PA_{kin}}$, and kinematic axial ratio q_{kin} ($= 1 - \varepsilon_{\mathrm{kin}}$). By default q_{kin} is constrained to the interval [0.1, 1], while we let $\mathrm{PA_{kin}}$ unconstrained.

The result of the kinemetric analysis of the velocity map from the cleaned data cube (Fig. 2.5) is listed in Table 2.2, and the left panel of Fig. 2.8 shows the kinemetry model velocity map. The Voronoi bin with the highest uncertainty was excluded from the model. From

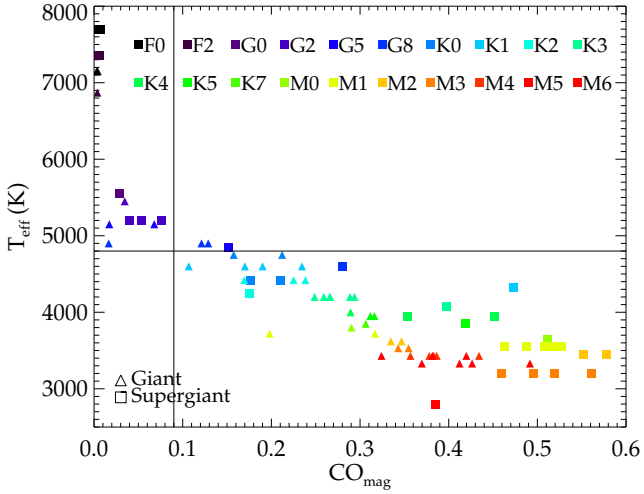

Figure 2.7: Relationship between effective temperature $T_{\rm eff}$ in K and the CO index $CO_{\rm mag}$ for giant (triangle symbol) and supergiant (square symbol) stars of the IRTF Spectral Library (Rayner et al. 2009). Different colours denote a different spectral type. The black horizontal line marks 4 800 K, the black vertical line marks $CO_{\rm mag}$ = 0.09

the axial ratio one can distinguish three families of ellipses. The three innermost ellipses form the first family, the next seven ellipses the second family, and the outermost five ellipses the third family.

For the two outer families the kinematic position angle $\rm PA_{kin}$ is $4 - 15°$ Galactic east of north, with a median value of 9°. However, the photometric position angle $\rm PA_{phot}$ was measured by Schödel et al. (2014a) using *Spitzer* data to ∼0°. This means that there is an offset between $\rm PA_{phot}$ and $\rm PA_{kin}$. To test whether this offset could be caused by extinction from the 20-km·s^{-1}-cloud (M-0.13-0.08, e.g. García-Marín et al. 2011) in the Galactic southwest, we flagged all bins in the lower right corner as bad pixels and repeated the analysis, but the position angle offset remained. We tested the effect of Voronoi binning by running kinemetry on a velocity map with S/N = 80. While the values of $q_{\rm kin}$ for the second family are by up to a a factor two higher with this binning, the $\rm PA_{kin}$ fit is rather robust. We obtained a median value for $\rm PA_{kin}$ of 12.°6 beyond a semi-major axis distance of r ∼40″. We conclude that the effect of the binning can vary the value of the $\rm PA_{kin}$, but the PA offset from the Galactic plane is robust to possible dust extinction and binning effects. Also our cleaning of bright stars and foreground stars may cause a bias in the $\rm PA_{kin}$ measurements. For comparison we ran the kinemetry on the velocity map of the full data cube (Fig. 2.4). In this case there is higher scattering in the kinemetric parameters, caused by shot noise. However, beyond 35″ semi-major axis distance the median $\rm PA_{kin}$ is at 6.°1, i.e. the PA offset is retained. This smaller value could come from the contribution of foreground stars, which are aligned along the Galactic

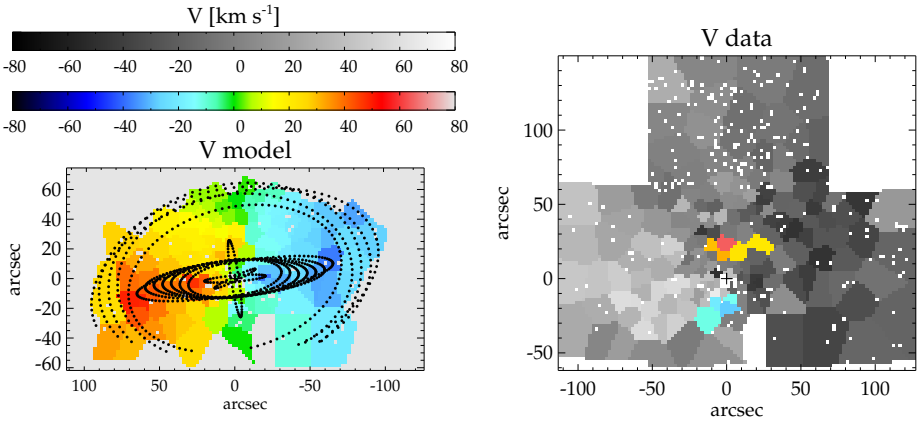

Figure 2.8: Left panel: Kinemetric model velocity map of the cleaned data cube. Black dots denote the best fitting ellipses. The model goes only to $r \sim 100''$ along the Galactic plane and to $\sim 60''$ perpendicular to it. Right panel: The velocity map as in Fig. 2.5 shown in grayscale, the bins that show rotation perpendicular to the Galactic plane are overplotted in colour scale.

plane. It could also mean that bright stars are not as misaligned to the photometric major axis as fainter stars are. Young stars tend to be brighter, thus the integrated light likely samples an older population than the individual stars. Analysis of the resolved stars in the colour interval $1.5\,\mathrm{mag} \leq H - K_S \leq 3.5\,\mathrm{mag}$ and in the radial range of $50''$ to $100''$ shows an offset in the rotation from the Galactic plane by $2\overset{\circ}{.}7 \pm 3\overset{\circ}{.}8$. As previous studies focused on the brightest stars of the cluster, the PA offset of the old, faint population remained undetected.

In the innermost family there is one ellipse with a position angle of $-81\overset{\circ}{.}5$, i.e. $\mathrm{PA_{kin}}$ is almost perpendicular to the photometric position angle $\mathrm{PA_{phot}} \approx 0^\circ$. This is caused by a substructure at $\sim 20''$ north and south of Sgr A*, that seems to rotate on an axis perpendicular to the Galactic major axis. This feature is highlighted in the right panel of Fig. 2.8. North of Sgr A* we find bins with velocities of 20 to $60\,\mathrm{km{\cdot}s^{-1}}$, while in the Galactic south bins with negative velocities around -10 to $-30\,\mathrm{km{\cdot}s^{-1}}$ are present. The feature expands over several Voronoi bins north and south of Sgr A*. It extends over $\sim 35''$ (1.4 pc) along the Galactic plane, and $\sim 30''$ (1.2 pc) perpendicular to it.

This substructure also causes the small axial ratio values of the second family of ellipses between $30''$ and $70''$ in our kinemetry model. All semi-minor axis distances from Sgr A* are below $20''$, i.e. at smaller distances to Sgr A* than the perpendicular substructure. Only the third family of ellipses, which has semi-major axis values above $70''$, skips over this substructure and reaches higher values of q_{kin}.

To check if the perpendicular rotating substructure is real, we applied Voronoi binning with a higher S/N of 80 instead of 60, and obtained again this almost symmetric north-south structure. Also with a lower S/N of 50, the substructure appeared in both data cubes. We also checked the influence of the cleaning from bright stars on this feature using the cleaned

Table 2.2: Result of the kinemetric analysis of the cleaned data cube velocity map. The columns denote the semi-major axis distance r in arcsec of the best fitting ellipses to Sgr A*, the kinematic position angle PA_{kin} in degrees, the kinematic axial ratio q_{kin}, and the rotation velocity V_{rot} in km·s^{-1}. The position angle is defined such that 0° corresponds to rotation around the Galactic North-South direction.

r [arcsec]	PA_{kin} [°]	q_{kin}	V_{rot} $\left[\mathrm{km \cdot s^{-1}}\right]$
15.0	25.2 ± 1.4	0.10 ± 0.00	30.5 ± 1.4
20.5	4.9 ± 2.0	0.10 ± 0.00	43.9 ± 1.1
26.1	−81.5 ± 1.3	0.10 ± 0.00	24.1 ± 1.4
31.7	9.1 ± 1.3	0.37 ± 0.01	38.5 ± 1.1
37.3	6.7 ± 1.2	0.34 ± 0.01	31.5 ± 0.9
43.1	4.4 ± 1.0	0.29 ± 0.01	32.2 ± 0.7
48.9	4.8 ± 1.0	0.25 ± 0.01	35.5 ± 0.6
54.7	4.8 ± 1.1	0.22 ± 0.01	37.4 ± 0.5
60.7	5.9 ± 1.0	0.20 ± 0.01	40.8 ± 0.5
66.8	9.0 ± 1.5	0.17 ± 0.02	46.8 ± 0.5
73.0	14.5 ± 0.5	0.65 ± 0.01	37.1 ± 0.6
79.3	7.0 ± 1.0	0.72 ± 0.02	29.7 ± 0.7
85.7	10.5 ± 1.1	0.74 ± 0.01	27.5 ± 0.8
92.3	10.2 ± 1.3	0.66 ± 0.01	32.1 ± 0.9
99.0	15.6 ± 1.1	0.57 ± 0.01	35.8 ± 0.9

maps with $K_{\rm cut}$ =11 mag and $K_{\rm cut}$ = 12 mag. The substructure remained also in these data cubes, independent of the applied binning. The fact that this feature persists independent on the applied magnitude cut, or binning, and that it extends over several bins, indicates that the observed kinematic structure is not caused by shot noise of individual stars.

We ran a Monte Carlo simulation to test if shot noise can mimic the observed substructure. We did this in 1 000 runs by adding random velocities to a smooth velocity map and running Kinemetry on the simulated velocity maps. Then we tested if there are substructures in the simulated velocity maps. First, we constructed a smooth velocity map using Kinemetry on the velocity map of the cleaned data cube. By constraining the $PA_{\rm kin}$ to the interval $[-25°, 25°]$ we obtained a velocity map without any substructures. To this smooth velocity map we added random velocities drawn from a normal distribution with a mean velocity of $0\,{\rm km\cdot s^{-1}}$, and a standard deviation of $\sigma = 8.2\,{\rm km\cdot s^{-1}}$. The value of $\sigma = 8.2\,{\rm km\cdot s^{-1}}$ is a measure for the shot noise (see Section 2.3.2). On 1 000 simulated velocity maps we ran Kinemetry models. Then we analysed if there are substructures in the simulated velocity maps. A substructure has to fulfil the following criteria: 1.) In the Kinemetry model there is an ellipse with a $PA_{\rm kin}$ that deviates by more than 45° from the median of the other $PA_{\rm kin}$ in this run; 2.) The velocity of this ellipse $V_{\rm rot}$ is greater than $8.2\,{\rm km\cdot s^{-1}}$. Our Monte Carlo simulation reveals that in 1,000 simulated velocity maps only 9.1 per cent have such a substructure. Only 0.2 per cent have a substructure with $V_{\rm rot}$ >20 ${\rm km\cdot s^{-1}}$, which is comparable to the value of $V_{\rm rot} = 24.1\,{\rm km\cdot s^{-1}}$ we find in the ISAAC data (see Table 2.2). We conclude that the feature is significant at 99.8 per cent and it is unlikely that a statistical fluctuation can mimic a kinematic substructure in our data.

We do not find a velocity substructure for the single bright stars as seen in the integrated light. In both the northern and the southern region, the median velocities are $\sim 3\,{\rm km\cdot s^{-1}}$, i.e. consistent with zero. We note that the bright stars likely represent different stellar populations than the unresolved light. The bright stars are dominated by younger populations with supergiants and AGB stars, while the unresolved light is dominated by older populations, where supergiants and AGB stars are rare. Thus this substructure, if real, would likely have an older stellar population. We discuss this discovery in more detail in Section 2.6.1.

The rotation velocity obtained by the Kinemetry model is at median values of $\sim 33\,{\rm km\cdot s^{-1}}$ for all different tested data cubes and binnings. The exact shape of the curve however depends on the fitted ellipse axial ratios, which varies with the binning of the velocity map.

2.4.2 Specific angular momentum λ_R

Emsellem et al. (2007) introduced the specific angular momentum λ_R to classify early-type galaxies in slow and fast rotators. This is a more robust classification criterion than the relation V/σ_e. We calculated the quantity λ_R for the first time for a nuclear star cluster. λ_R is a dimensionless parameter that quantifies the observed projected stellar angular momentum per unit mass. To compute λ_R we used the two-dimensional spatial information from the kinematic maps, weighted by the luminosity. Slow rotators have values of $\lambda_R < 0.1$ within

their effective radius $r_{\rm eff}$, while fast rotators have values above 0.1. We calculated λ_R using Equation 6 of Emsellem et al. (2007):

$$\lambda_R = \frac{\sum_{i=1}^{N_p} F_i R_i |V_i|}{\sum_{i=1}^{N_p} F_i R_i \sqrt{V_i^2 + \sigma_i^2}} \tag{2.2}$$

Here i runs over all pixels of the data cube, F_i is the flux in the $i-$th pixel, R_i is its distance to Sgr A*, V_i and σ_i are the velocity and velocity dispersion in the pixel. To compute λ_R we used the SIRIUS image and transformed it to the same pixel size and astrometry as the data cubes for luminosity weighting. We used the kinematic maps from the cleaned data cube, and summed within ellipses with ellipticity $\varepsilon = 0.29$. This is the photometric ellipticity found by Schödel et al. (2014a) in *Spitzer* mid-infrared data. The resulting λ_R profile is shown in Fig. 2.9, where r is the mean radius of the ellipses, and $r_{\rm eff} = 4.2$ pc ($110''$, Schödel et al. 2014a). Assuming a smaller value for ε decreases λ_R and the slope of λ_R, but even with $\varepsilon = 0$, we obtain $\lambda_R > 0.2$ for all radii.

The specific angular momentum is used to classify galaxies as fast and slow rotators. Emsellem et al. (2011) found that fast rotators have $\lambda_R > k_{FS} \times \sqrt{\varepsilon}$, where k_{FS} is a scaling parameter. k_{FS} is 0.31 when using λ_{R_e}, i.e. λ_R at one effective radius $r_{\rm eff}$. This means a value of $\lambda_{R_e} > 0.16$ would be expected for a fast rotator with an ellipticity of 0.29. For the Milky Way nuclear star cluster $r_{\rm eff}$ is ~4.2 pc (Schödel et al. 2014a). At our outermost ellipse radius of 3.5 pc we obtain $\lambda_R \approx 0.36$ with $\varepsilon = 0.29$. So the Milky Way nuclear star cluster has similar rotational support as fast rotating elliptical galaxies have. A comparison with Fig. 5 of Emsellem et al. (2007) shows that λ_{R_e} is below the value expected for an isotropic oblate rotator. This suggests that the Milky Way nuclear star cluster has anisotropic kinematics at large radii.

2.4.3 Radial profiles

In this section we study the kinematics of the nuclear star cluster by applying different binnings to the data cubes and compute profiles. We investigate the rotation curve and compare our findings to previous results.

When we plot the projected distance of each Voronoi bin from Sgr A* along the Galactic plane against the velocity of each bin, we obtain a position-velocity diagram, which is shown in Fig. 2.10 for both data cubes. From the data cube containing only faint member stars (red circle points), we deduce that the maximum rotation velocity is about $50\,{\rm km\cdot s^{-1}}$. For the outer fields, the rotation is flatter. Only one of the six data points has a velocity higher than $36\,{\rm km\cdot s^{-1}}$.

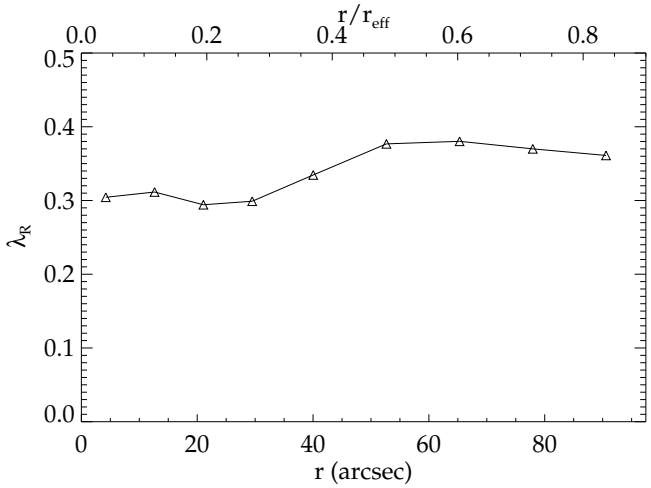

Figure 2.9: The specific angular momentum λ_R profile calculated in ellipses with ellipticity $\varepsilon = 0.29$ (Schödel et al. 2014a), and plotted against the mean radius of the ellipses. The upper x-axis of the plot displays the ratio of $r/r_{\rm eff}$, where $r_{\rm eff}$ is the effective radius ($r_{\rm eff} = 4.2$ pc, Schödel et al. 2014a).

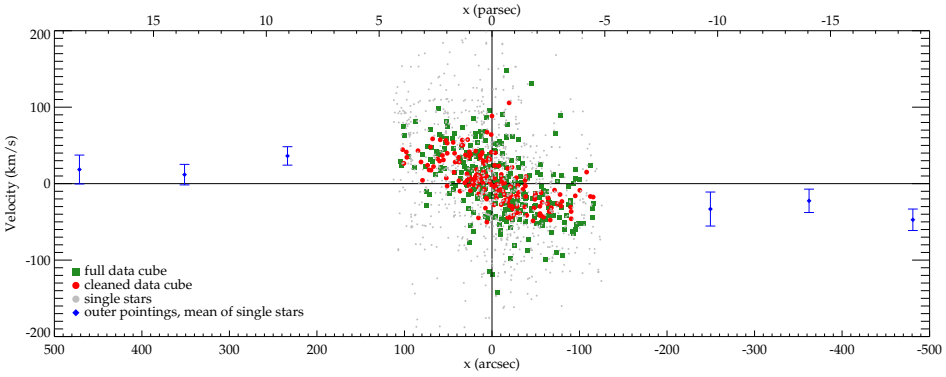

Figure 2.10: Position-velocity diagram along the Galactic plane for the velocity maps of Fig. 2.4 and 2.5. Results from our full ISAAC data cube are shown as green rectangles, red circles show the result from the cleaned data cube, which contains only faint cluster member stars. Grey dots denote velocity measurements from single stars, the blue diamonds are the mean velocities of the bright stars at the outer fields, corrected for perspective rotation.

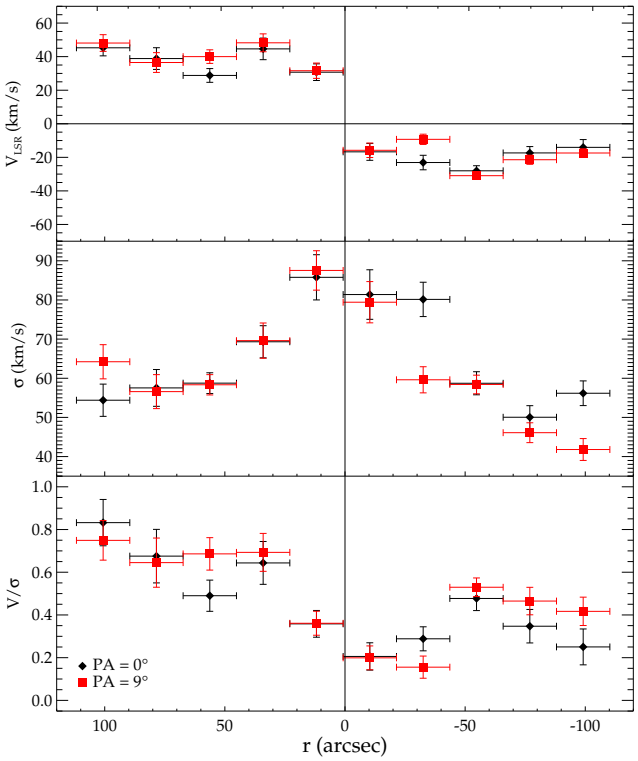

Figure 2.11: Velocity profile, velocity dispersion σ, and V/σ for a 22″ broad slit along the Galactic plane from the cleaned data cube (black diamonds), and for a slit tilted by 9° counterclockwise with respect to the Galactic plane (red square symbols).

For further analysis we did not use the Voronoi binned velocity maps of Fig. 2.4 and 2.5, but directly binned the data cubes in major axis bins and radial annuli. In order to derive the kinematics along the photometric major axis only, we binned the cleaned data cube in rectangles, which extend over ∼22″ perpendicular to the Galactic plane, i.e. ∼11″ towards the Galactic North and South of Sgr A*. Each rectangle is 22″ broad in Galactic east-west direction. This resembles a slit along the Galactic plane, centred on Sgr A* that is 22″ wide. We summed the spectra in the rectangular bins and fitted the CO absorption lines with pPXF. The resulting velocity and velocity dispersion profiles are shown in Fig. 2.11 as black diamonds, together with the V/σ profile. Alternatively we rotated the slit axis by 9°, which is our median kinematic position angle offset found in Section 2.4.1, and applied a similar binning. The result is shown as red square symbols in Fig. 2.11.

We obtained a rotation curve with an amplitude of ∼40 km·s^{-1}. As expected, the absolute velocity values are generally higher using the tilted slit than using a slit along the Galactic plane. Further, the absolute velocities are higher on the eastern side than on the western

Table 2.3: Profile of the root-mean-square velocity $V_{\rm rms}$ as shown in Fig. 2.12. r is the distance from Sgr A* in arcsec, $V_{\rm rms}$ values are in km·s^{-1}.

r [arcsec]	$V_{\rm rms}$ $\left[\mathrm{km \cdot s^{-1}}\right]$ full data cube	$V_{\rm rms}$ $\left[\mathrm{km \cdot s^{-1}}\right]$ cleaned data cube
1.5	179 ± 20	166 ± 20
4.0	14 ± 2	136 ± 21
7.5	105 ± 8	98 ± 10
12.5	78 ± 4	73 ± 5
20.0	78 ± 3	84 ± 4
32.5	78 ± 4	71 ± 3
62.5	65 ± 2	67 ± 3
77.5	65 ± 2	62 ± 3
92.5	69 ± 2	67 ± 3
107.5	69 ± 2	61 ± 3
122.5	71 ± 3	69 ± 5
255	75 ± 3	58 ± 4
355	49 ± 4	77 ± 5
455	78 ± 3	74 ± 4
	single stars	
241	87 ± 9	
357	67 ± 7	
455	79 ± 9	

side by more than 10 km·s^{-1}. The velocity dispersion rises only to ~90 km·s^{-1}. This can be explained by the fact that the velocity dispersion map (Fig. 2.5) has values higher than 100 km·s^{-1} only in few small bins in the very centre ($r \lesssim 10''$). The V/σ has a minimum close to the centre, where the velocity dispersion is highest, and higher values at larger radii. At outer radii ($r > 50'' \approx 2$ pc), closer to the effective radius, we obtain V/$\sigma \approx 0.6$. The value of V/σ at the Galactic West is smaller than at the Galactic East, as also the absolute values of the velocities are lower.

We also computed a velocity dispersion profile within circular bins around Sgr A*. The spectra in each bin were summed up and we computed the LOSVD with pPXF. The second moment is then the root-mean-square velocitiy, $V_{\rm rms} = \sqrt{V^2 + \sigma^2}$. The result is shown in Fig. 2.12 and listed in Table 2.3, the outermost data points are from our outer fields. Green rectangles denote the result from the full data cube, red circle points from the cleaned data cube. The difference between the two data cubes is mostly within the measurement uncertainties. The largest differences occur due to contamination of IRS 7 in the bin at 4″ and another

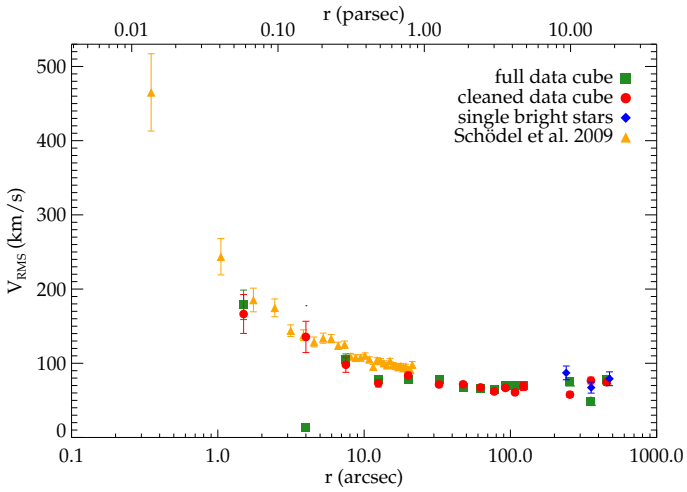

Figure 2.12: Velocity dispersion profile, obtained using circular bins around Sgr A*. The green rectangles are the data points from the full data cube, red circle points from the cleaned data cube. The large discrepancy at $r \sim 4''$ is due to the influence of the star IRS 7 on the green point. Blue diamonds are obtained from single bright stars in the outer fields. Orange triangles are proper motion data from Schödel et al. (2009).

bright star at a radius of $360''$. Most stars in the centre of the nuclear star cluster are young and do not show strong CO absorption lines that we use for our kinematic measurements. This means that the velocity dispersion we measure for the central points comes mostly from stars that lie only in projection close to Sgr A*, and the velocity dispersion at $r \lesssim 8''$ is a lower limit (Sellgren et al. 1990; Haller et al. 1996).

The surface brightness at the outer fields is lower than in the central field. After cleaning the data from bright stars and foreground stars, the S/N of the outer fields is rather low. On the other hand, bright stars can severely effect the result from the full data in the outer fields. Therefore we computed $V_{\rm rms}$ as a third approach from the bright stars we cut out, corrected for perspective rotation (see Section 2.3.2). This has the advantage that all stars have the same weight, irrespective of their magnitude. The results from the three approaches agree quite well at $8'$; at $4'$ and $6'$ there is more scattering.

For the central $20''$ we also plot the proper motion data of Schödel et al. (2009) for comparison (orange triangles). To extract these data along a radial profile we made circular bins around Sgr A*. Then we computed the mean velocity and velocity dispersion of each bin using a maximum likelihood approach described in Pryor & Meylan (1993). In contrast to computing the mean and standard deviation of the data, this method takes the different uncertainties for the velocity measurements into account. We used the velocities perpendicular and parallel to the Galactic plane. Each bin contains at least 21 stars. We found that the velocity dispersion perpendicular to the Galactic plane σ_b is in better agreement with our LOSVD

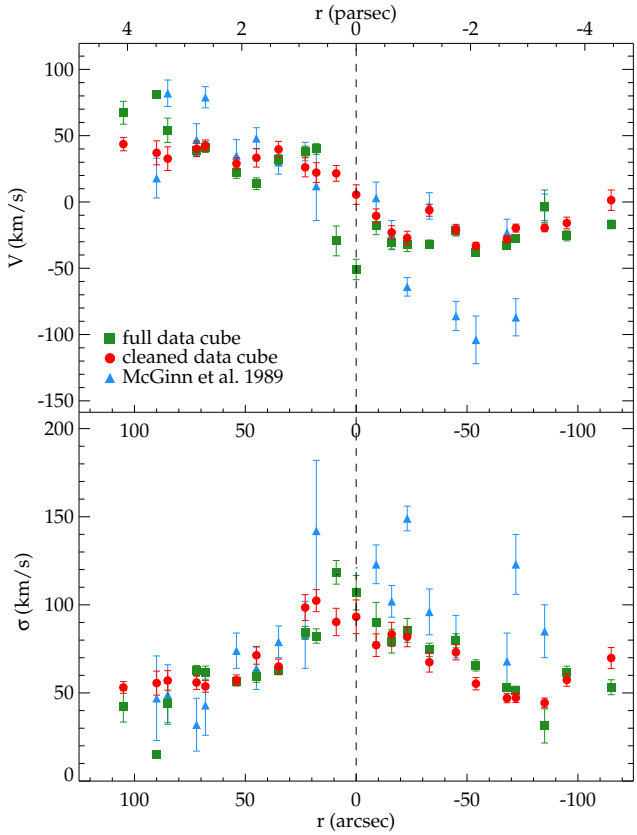

Figure 2.13: Velocity (upper panel) and velocity dispersion profile (lower panel) along the major axis, with IRS 16 as the centre. We applied the binning of McGinn et al. 1989 (blue), extended by five additional binning apertures. Results from our full ISAAC data cube are shown as green rectangles, red circles show the result from the cleaned data cube, and blue triangles denote the data from McGinn et al. (1989).

data than the velocity dispersion parallel to the Galactic plane σ_l. Parallel to the Galactic plane the velocity dispersion is higher than perpendicular to it (see Fig. 6 of Schödel et al. 2009).

The only previous observations of the Galactic centre in integrated light are from McGinn et al. (1989). They had a circular aperture of 20″ diameter, and measured velocity and velocity dispersion profiles along the major axis (McGinn et al. 1989, Figs. 1, 4, and 5) using the first CO band head. To compare our work with these early results, we binned our data cube in exactly the same way as McGinn et al. (1989). As centre we used IRS 16C (α = 266.°41705, δ = −29.°007826, Henry et al. 1984), as McGinn et al. (1989) did. We applied four additional binnings which were not covered by McGinn et al. (1989). The resulting profiles are displayed in Fig. 2.13, where the upper panel is the velocity V, and the lower panel is the velocity dispersion σ, both in km·s^{-1}. The profiles from the cleaned data cube appear smoother than the profiles from the full data cube, as the data is less affected by shot noise of dominant bright stars which can produce outliers. One such example is the bright supergiant IRS 7. This star has a big effect on the integrated spectrum in the bins centred at r = −9″ and 0″. Cutting out only the star IRS 7 from the data cube containing all stars decreases the velocity measurement by more than 30 km·s^{-1}, while the velocity dispersion changes by only ∼14 km·s^{-1}. Using smaller apertures, this single bright star can affect the results even more. The data of McGinn et al. (1989) has more outliers and extreme velocity variations than our data, especially to the western side of Sgr A*. Schödel et al. (2009) suggested that the data of McGinn et al. (1989) may sample two different stellar populations at different depth. Then their data could hint at two distinct rotating systems in the nuclear star cluster. Our data does not confirm this large scatter in the velocity and velocity dispersion, and the profiles have a rather smooth shape. Four velocity measurements of McGinn et al. (1989) on the western side of Sgr A* have significantly higher absolute values than our data has, while the other five measurements agree with our data. They confirm that the absolute values of the velocities on the western side are lower than on the eastern side of Sgr A*. On the western side the extinction is higher than on the eastern side.

2.4.4 Distribution of young stars

We computed the CO index $CO_{\rm mag}$ for our sample of bright stars as defined in Section 2.3.3. Figure 2.14 shows the distribution of the CO index for all bright member stars. The value of $CO_{\rm mag}$ roughly correlates with the age of the stars, this means that blue data points denote stars that are more likely to be younger than stars shown in red colours. Blue filled star symbols denote stars with $CO_{\rm mag} < 0.09$, indicating stars younger than 300 Myr. We note that the presence of foreground extinction would mean the stars we are sampling are even brighter and thus younger. Most of the 26 young stars are within 1 pc of the nuclear star cluster, confirming previous studies. For example, five of our stars lie within 0.″3 distance of stars listed by Paumard et al. (2006). A comparison with the young star candidates of Nishiyama & Schödel (2013) results in seven matches. One of those matches has no counterpart in any previous spectroscopic study yet. Its colour in $H - K_S = 1.5$ mag, which is at our limit for

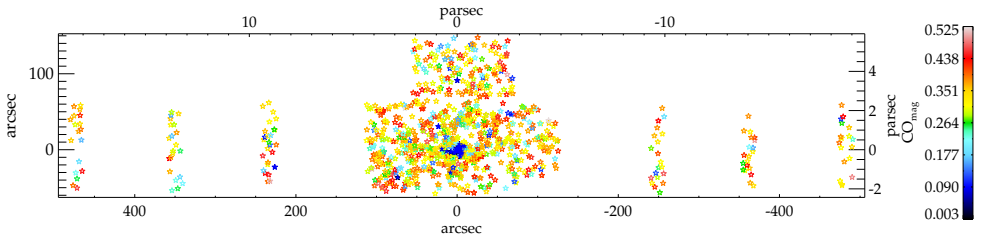

Figure 2.14: CO index map of 1 153 bright stars ($K_S \leq 11.5$ mag) with S/N >12. Filled blue star symbols denote stars with $CO_{\rm mag} < 0.09$, which are younger than 300 Myr.

foreground stars. At greater distance from Sgr A*, there are only few stars with $CO_{\rm mag} < 0.09$, and none at our outer fields at 360″ and 480″. But as the covered area beyond 350″ is only about 2.1 arcmin^2, we might simply miss the young stars.

It is possible that the young star candidates are foreground stars, although their colours in $H - K_S$ are at least 1.5 mag, and for 20 of the stars even more than 2.1 mag. The intrinsic $H - K_S$ colour for O to A type stars is about −0.1 to 0.05 (Straižys & Lazauskaitė 2009), therefore the measured colour is almost entirely caused by extinction. Schödel et al. (2010) and Fritz et al. (2011) found mean extinction values of A_H = 4.21 mag to 4.48 mag and A_{K_S} = 2.42 mag to 2.74 mag in the central region of the Galaxy. Extinction varies on arcsecond scale with a standard deviation of 0.3 mag in A_{K_S} (Schödel et al. 2010). Thus the measured colours are consistent with these stars being located in the Galactic center.

One problem of our limited spectral range is that stars with low velocities $<-250\,{\rm km\cdot s^{-1}}$ can be misidentified as a star with a low CO index. We found three such stars, which are not included in our sample of young star candidates. Observations with larger spectral range are necessary to confirm the spectral type of these stars and give a better estimation of their age.

2.5 Dynamical modelling

To measure the mass of the Milky Way nuclear star cluster and black hole we dynamically model our kinematic data. We apply axisymmetric Jeans models (Jeans 1922) to our kinematic data. We use the IDL program package Jeans Anisotropic MGE dynamical models (JAM) written by Cappellari (2008). In Section 2.5.1 we fit a surface brightness profile. We present the results of the Jeans models in Sections 2.5.2. Our mass profile is shown in Section 2.5.3.

2.5.1 Surface brightness profile

Light indicates the stellar density, and for a constant mass-to-light ratio (Y) also the gravitational potential of a stellar system. For the Jeans models we require a surface brightness profile. We used mid-infrared data to determine the surface brightness profile, as the interstellar extinction towards the Galactic centre reaches a minimum at ∼3−8 μm (Fritz et al. 2011).

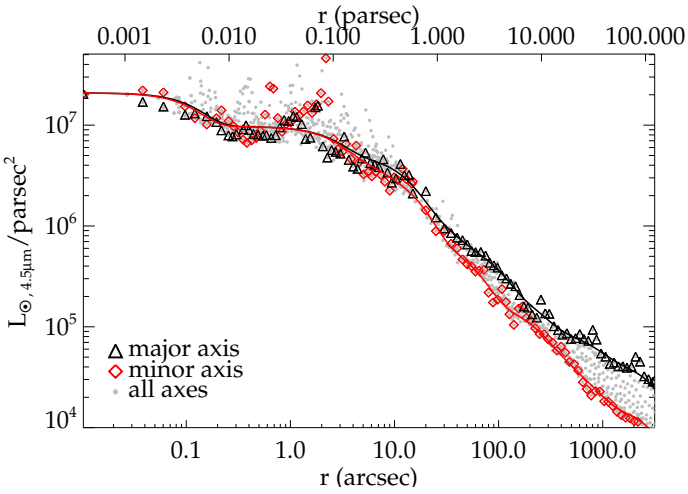

Figure 2.15: Surface brightness profile derived from a dust and extinction corrected *Spitzer*/IRAC 4.5 μm image and NACO K_S-band mosaic for the central 30″. Black triangles denote measurements along the major axis, and red diamonds along the minor axis, the grey data points are all measurements, at all axes. The spikes in the profile are due to individual bright stars. Solid lines illustrate the Multi-Gaussian Expansion (MGE) fit to the data.

We derived a surface brightness profile using imaging data from *Spitzer*/IRAC (Stolovy et al. 2006) at 4.5 μm. The image was dust and extinction corrected, and smoothed to a pixel scale of 5″ ·pixel^{-1}. For details about the correction steps we refer to Schödel et al. (2014a). For the centre, we used a NACO K_S-band mosaic (Schödel et al. 2009) covering 40.″5 × 40.″5 scaled to the flux of the 4.5 μm *Spitzer* image, with a pixel scale of 0.″027·pixel^{-1}.

We used the MGE_FIT_SECTORS package. This is a set of IDL routines written by Cappellari (2002) to do photometric measurements directly on images and apply a Multi-Gaussian Expansion (MGE, Emsellem et al. 1994) fit to parameterise a surface brightness profile. The photometry of the two images was measured, and we determined a scale factor using the overlap region of the two images to convert the NACO image to the *Spitzer* flux. Then photometry was measured on each image along 12 angular sectors. The routine assumes four-fold symmetry and averages the measurements of four quadrants, taken along elliptical annuli with constant ellipticity ε.

A set of two-dimensional Gaussian functions was fitted to the combined photometric measurements. Therefore we also took the PSF of the NACO image into account. The MGE fit is not designed for a structural decomposition of the Galaxy's light profile. But Gaussians have the great advantage that deprojection can be done analytically. This procedure has been used already for galaxies (e.g. Cappellari et al. 2006), nuclear clusters (e.g. Seth et al. 2010), and globular clusters (e.g. Lützgendorf et al. 2012; Feldmeier et al. 2013). We assumed the position of Sgr A* as centre and excluded the dark 20-km·s^{-1}-cloud and the Quintuplet cluster from the *Spitzer* image. As the central region of the 4.5 μm emission is dominated by

Table 2.4: The Multi-Gaussian Expansion (MGE) fit parameters for the 4.5μm *Spitzer*/IRAC dust and extinction corrected image in combination with the NACO K_S-band mosaic scaled to *Spitzer* flux. I is the peak surface brightness, $\sigma_{\rm MGE}$ is the standard deviation, and q is the axial ratio of the Gaussian components.

I $\left[10^5 L_{\odot,4.5\mu\mathrm{m}} \cdot \mathrm{pc}^{-2}\right]$	$\sigma_{\rm MGE}$ [arcsec]	q
112	0.1	0.9
46.2	2.1	1.0
16.0	8.4	0.6
20.4	11.5	1.0
7.48	22.8	0.7
4.53	66.4	0.7
0.77	143	1.0
0.73	184	0.2
0.47	581	0.4
0.17	2705	1.0
0.31	2705	0.2

the mini-spiral and not by stellar emission, we also excluded pixels within 0.6 pc distance to Sgr A* of the *Spitzer* image from photometry measurements. The flux scaled NACO image was used out to 15″ distance from Sgr A*. Table 2.4 lists the output of the MGE fit. The last two Gaussian components have the same value of $\sigma_{\rm MGE}$, as they are close to the edge of the image. Figure 2.15 shows the MGE surface brightness profile along the major and minor axes.

2.5.2 Axisymmetric Jeans models

For the axisymmetric Jeans models we used the surface brightness parametrisation of Table 2.4 as an input. We assume dan inclination angle of 90°, i. e. the Galaxy is seen edge-on. We fitted the model to the kinematic data. For this purpose we used the velocity maps of Fig. 2.5 of the faint stellar population, and excluded the bin with the highest uncertainty and lowest S/N. From these maps we computed the root-mean-square velocity $V_{\rm rms} = \sqrt{V^2 + \sigma^2}$ for each bin. In all models we assumed a constant mass-to-light ratio Y. All Y values are for 4.5 μm and in units of $M_\odot / L_{\odot,4.5\mu\mathrm{m}}$.

For the anisotropy β (= $1-\overline{v_z^2}/\overline{v_R^2}$, Cappellari 2008) we tested different assumptions. We assumed isotropy in the central 0.5 pc (Do et al. 2013b), but fitted the anisotropy further out. Therefore we assumed different radial shapes of the anisotropy β: 1) constant anisotropy beyond 0.5 pc; 2) logarithmically increasing anisotropy beyond 0.5 pc, i.e. $\beta \propto \log(r + 0.5\,\mathrm{pc})$; 3) linear increasing anisotropy beyond 0.5 pc, i.e. $\beta \propto r$. We have three fit parameters:

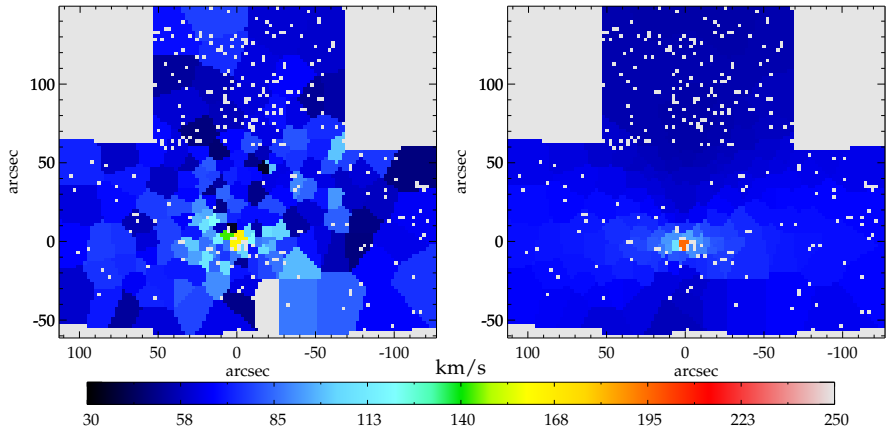

Figure 2.16: Result of the two-dimensional Jeans model with anisotropy $\beta_{\rm const} = -0.3$, mass-to-light ratio Y = 0.56, and black hole mass $M_\bullet = 1.7 \times 10^6\, M_\odot$. The left panel shows ISAAC data of the cleaned cube, for the root-mean-square velocity $V_{\rm rms} = \sqrt{V^2 + \sigma^2}$, and the right panel is the best-fit model. The grey pixels mark regions, which contain no information. One bin was excluded from the fit due to its high uncertainty and low signal-to-noise, and it is also shown in grey on the left panel.

Y, $\beta_{100\rm pc}$, and the black hole mass $M_\bullet$. As a fourth approach, we assumed constant anisotropy over the entire cluster and did not constrain the central 0.5 pc to be isotropic and fitted Y, $\beta_{\rm const}$, and the black hole mass $M_\bullet$. We limited the value of β to [-4; 0.9], since lower and higher values seem to be unrealistic.

Our best fit model has constant tangential anisotropy, the best fit parameters are $\beta_{\rm const} = -0.3^{+0.3}_{-0.4}$, Y = $0.56\ ^{+0.22}_{-0.26}$, and $M_\bullet = (1.7\ ^{+1.4}_{-1.1}) \times 10^6\, M_\odot$, with $\chi^2_{\rm red} = 12.5$. The uncertainties are the 68 per cent confidence limits. Data and model are shown in Fig. 2.16. The left panel is the data, the right panel displays the best-fit model.

The results quoted here are from models without PSF convolution as the effect is negligible in our low spatial resolution data. In order to test this assumption we performed a PSF convolution with the seeing of the ISAAC data and found a difference that was less than 10 per cent of the uncertainties. A variation of the inclination angle to 80° has no effect on the best fit results, but increases $\chi^2_{\rm red}$ slightly.

The different β-profiles obtain consistent results for Y and $M_\bullet$, with only slightly higher values of $\chi^2_{\rm red}$ (13.0−13.4). This suggests that we cannot constrain a possible β variation over the cluster radius with our Jeans models. There is not much difference in the results if we run our models with the six outer fields or without. Using the kinematic maps containing all stars (Figure 2.4), the tangential anisotropy is increased ($\beta_{100\rm pc}$ and $\beta_{\rm const} \leq -0.5$), the best fit Y is lower (∼0.32), and the black hole mass is slightly higher ($\sim 2.2 \times 10^6\, M_\odot$). Differences to the results from the kinematic map of the cleaned data cube are less than the uncertainty limits. The $\chi^2_{\rm red}$ is much higher with values between 235 and 242, since the kinematic map of the full data cube is more affected by shot noise caused by single bright stars.

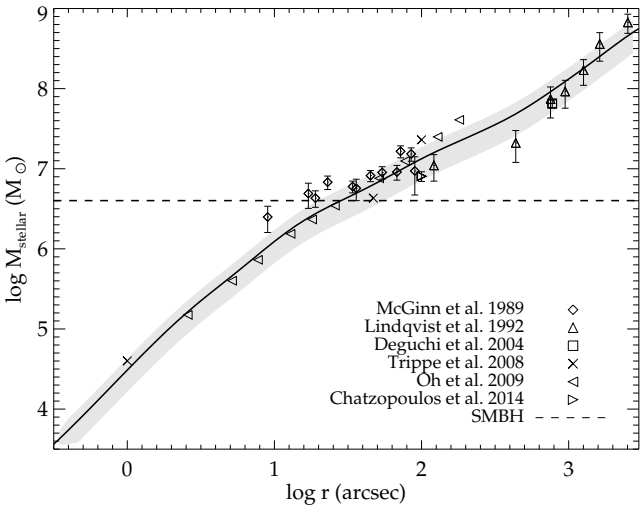

Figure 2.17: Enclosed stellar mass within a distance of 0.3″ to 50′ along the mean radius of the ellipses in units of $M_\odot$ and in logarithmic scaling. The black line denotes a Υ value of 0.56, the grey shaded contours show the uncertainty in Υ of $^{+0.22}_{-0.26}$. The horizontal line is for a supermassive black hole with the mass $M_\bullet = 4 \times 10^6\ M_\odot$. We also plot the results for the enclosed mass from previous studies: McGinn et al. (1989, assumed Galactocentric distance R_0 = 8.5 kpc), Lindqvist et al. (1992a, R_0 = 8.5 kpc), Deguchi et al. (2004, R_0 = 8 kpc), Trippe et al. (2008, R_0 = 8 kpc), Oh et al. (2009, R_0 = 8 kpc) and Chatzopoulos et al. (2015a, R_0 = 8.3 kpc).

As the population in the central parsec ($r \approx 13''$) is younger than at larger distances from Sgr A*, this might influence the result of the Υ. We tested this by running the Jeans model without the $V_{\rm rms}$ data points inside $r = 10''$ and $r = 20''$. In both cases there is no difference in the best fit values of Υ, $M_\bullet$ and β. As another test we set the Υ of the innermost five Gaussian components ($\sigma_{\rm MGE}$ <0.9 pc) to zero before we run the Jeans models. This results in an increase of the Υ of the outer components to 0.7 and $M_\bullet$ to $3.4 \times 10^6\ M_\odot$. The value of Υ is within the uncertainty limits, while the black hole mass fit is significantly improved. But even with such an extreme assumption of Υ = 0 in the central parsec, the black hole mass is too low. When we force the black hole mass to be $4 \times 10^6\ M_\odot$, the best-fit value of Υ is 0.35 and $\beta = -0.3$. This is within our uncertainties for Υ.

2.5.3 Mass profile

With the mass-to-light ratio and our surface brightness profile we computed the enclosed mass of the nuclear star cluster. The light profile is parameterised by a series of Gaussians,

which is given in Table 2.4. This profile is valid out to 100 pc distance from Sgr A*. We computed the enclosed light within ellipses for each Gaussian component with the equation

$$L_j = 2\,\pi\, I_j\, \sigma^2_{\mathrm{MGE},j}\, q_j \left(1 - \exp\left(-\frac{x^2_{\max}}{2\sigma^2_{\mathrm{MGE},j}}\right)\right), \tag{2.3}$$

where $x_{\max}$ is the semi-major axis distance from the centre, up to which we integrate the light. Figure 2.17 illustrates the enclosed mass as a function of the mean radius of an ellipse $r = x_{\max} \times \sqrt{1-\varepsilon}$ with $\varepsilon = 0.29$ for a Υ of $0.56^{+0.22}_{-0.26}$. This is the best fit result of Section 2.5.2. The uncertainty of our light profile, which we get from the uncertainty map of the *Spitzer* image, has about the same effect on the enclosed mass profile as a Υ variation of 0.1.

At a distance of 10 pc from Sgr A*, the nuclear star cluster is still the dominant component of the Galaxy (Launhardt et al. 2002), it contributes more than the nuclear stellar disc. We obtain an enclosed mass of $(3.0^{+1.2}_{-1.4}) \times 10^7\ M_\odot$ at a mean distance of 10 pc. While this mass is an extrapolation from the area where we have good sampling of the kinematics, it is more robust than previous dynamical estimates (McGinn et al. 1989; Lindqvist et al. 1992a; Trippe et al. 2008; Schödel et al. 2009).

2.6 Discussion

2.6.1 Clues to the formation of the Milky Way nuclear star cluster

Our velocity maps of the Milky Way nuclear star cluster reveal two unexpected features: (1) the offset of the rotational position angle from the Galactic plane and photometric position angle of the nuclear star cluster, and (2) indications for the presence of a rotating substructure at $r \sim 0.8$ pc rotating perpendicular to the Galactic plane.

Our kinemetric analysis of the velocity map in Section 2.4.1 revealed an offset between the photometric and the kinematic position angle with a median value of $9° \pm 3°$ Galactic east of north. The photometric position angle is at $\sim 0°$ (Schödel et al. 2014a). The misalignment between kinematics and morphology suggests that the overall luminosity profile is dominated by a different stellar population than the kinematics. The exact value of the position angle offset depends on the binning of the velocity map, and we use these variations for our uncertainty. Kinematic misalignment larger than 10° was already observed for galaxies of the SAURON project by Krajnović et al. (2008), but mostly in triaxial, slow-rotating galaxies. In fast-rotating galaxies, kinematic misalignment is only observed in combination with triaxial structures like bars or shells, or in the very centre of the galaxy.

In a first order approximation, the potential is spherically symmetric because a supermassive black hole is embedded in the nuclear star cluster. In a spherically symmetric system stellar orbits are approximately planar rosettes at all orientations. But the sense of rotation of some stars on inclined orbits could be reversed. Then one would observe an asymmetric velocity field. The same is valid for triaxial or flattened potentials. Triaxial tumbling systems that extend beyond the radius of influence of a central black hole have different sequences of

orbits (Heisler et al. 1982). If those orbits are populated equally, the system can be in dynamical equilibrium (Schwarzschild 1982). Then the velocity field appears symmetric relative to the short axis when observed from the Sun's position inside the Galactic disc. However, asymmetries can be observed if a subset of inclined stellar orbits is preferentially populated.

Further, there appears to be a substructure that is red-shifted to the Galactic North ($V \approx 35\,\mathrm{km{\cdot}s^{-1}}$), and blue-shifted to the Galactic South ($V \approx -25\,\mathrm{km{\cdot}s^{-1}}$). This substructure rotates approximately perpendicular to the large scale sense of rotation. The sense of rotation of the well defined clockwise disc (e.g. Levin & Beloborodov 2003; Lu et al. 2009; Bartko et al. 2009; Yelda et al. 2014) is approximately opposite to the rotation we see in our data. But as we observe rather old stars, which show CO absorption lines, and the clockwise disc is seen in young stars, we do not expect the same dynamical properties.

Tremaine et al. (1975) suggested that nuclear star clusters form from infalling globular clusters. The kinematic misalignment and the perpendicular substructure could be the debris of such accretion events. Antonini et al. (2012) give a formula for the disruption radius r_{disr} at which an infalling massive star cluster is disrupted due to tidal stresses from the supermassive black hole (SMBH) in the nuclear star cluster. They found $r_{\mathrm{disr}} \approx 1\,\mathrm{pc}$ for the Milky Way nuclear star cluster, which is roughly equal to the core radius r_c of the old stellar distribution (0.5 pc, Buchholz et al. 2009). Antonini (2013) used an analytical model for globular cluster infall and found that the initial mass of the infalling clusters has to be at least $10^7\,M_\odot$ to penetrate to a galactocentric radius of ∼2 pc. However, this model neglects internal dynamics of the infalling cluster like e.g. mass segregation. Taking this into accout allows the infalling cluster to bring stars even closer to the centre (Antonini 2014). Therefore a substructure at ∼0.8 pc, like the one our data indicates, could be the remnant of a tidal disruption event.

Antonini (2014) ran N-body simulations to investigate the consecutive inspirals of 12 clusters to a Galactic centre. In this simulation only the orbits of stars from the first seven infalling clusters are close to isotropic at the end of the simulations. This is not the case for the orbits of stars from the last infalling clusters. After ∼3 Gyr the stellar orbits are still largely correlated, and would require about 10 Gyr to reach a fully isotropic distribution (F. Antonini, personal communication, April 2014). The relaxation time of the nuclear star cluster is several Gyr at all radii, and outside of 1 pc, the relaxation time is even longer than the age of the universe (Merritt 2010). Therefore we expect the signatures of infalling clusters to remain coherent over a long period of time.

Our observation of a kinematic misalignment and a perpendicular rotating substructure can be explained by the accretion of massive star clusters. This would support the theory that the accretion of massive stellar cluster plays a role in the formation of nuclear star clusters. We plan follow-up observation with KMOS (VLT) to verify these discoveries.

2.6.2 Underestimation of the black hole mass

Our two-dimensional Jeans models in Section 2.5 resulted in a black hole mass that is lower by a factor ∼2 than the result from direct measurements of $\sim 4 \times 10^6\,M_\odot$ (Ghez et al. 2008; Gillessen et al. 2009b). Before those measurements, the black hole mass was underestimated

by other studies as well (McGinn et al. 1989; Krabbe et al. 1995; Haller et al. 1996; Genzel et al. 1996).

As shown in Fig. 2.12, the ISAAC data velocity dispersion values are lower than the proper motion data of Schödel et al. (2009). This could be due to a bias in the measurement of the velocity dispersion in the ISAAC data, and cause the underestimation of the black hole mass. We derive the kinematics from the radial velocities of old stars only, and cannot trace the young population of stars in the centre. Therefore the measured velocity dispersion is mostly from stars that lie at a large distance in front and behind of Sgr A*, and only appear to be close to the SMBH in projection (Sellgren et al. 1990). This means that the measured velocity dispersion of the central ~8″ (0.3 pc) is rather too low (e.g. Haller et al. 1996).

But as the radius of influence of the black hole extends out to 2.3 pc (~60″, see Section 2.6.3) and the young stellar population extends only to 0.5 pc, this may not the only reason for the too low black hole mass. To test this assumption we excluded the kinematic data of the centre out to 0.8 pc (20″) and found no changes in the best-fit parameters of the Jeans models. We also considered the extreme and unphysical case that the value of the mass-to-light ratio Υ is zero for the Gaussian components of the potential with $\sigma_{\rm MGE} \leq 0.8$ pc. This is motivated by the fact that the Υ of young stars, which are in the central 0.5 pc, is lower than the Υ of old stars. This increased the black hole mass, but only to $3.4 \times 10^6\ M_\odot$.

Therefore the stellar population change alone cannot explain the too low black hole mass. The position angle offset may also have an effect on the black hole mass measurement in the two-dimensional Jeans models. Further, there might be a systematic bias in black hole mass measurements obtained with integrated light measurements, leading to an underestimation of black hole masses also in some other galaxies. We plan to investigate this issue in more detail in a follow-up paper.

2.6.3 Mass profile of the cluster

We obtain the cluster mass from the surface brightness assuming a constant Υ. As the stellar population in the nuclear star cluster is not uniform, this may be an oversimplification. But population synthesis models showed that, compared to optical light, the mid-infrared mass-to-light ratio is rather constant. Under this assumption, McGaugh & Schombert (2013) found a mean value of $(0.5 \pm 0.1)\ M_\odot / L_{\odot,3.6\mu\rm m}$ in disc galaxies. Meidt et al. (2014) constrained the mean value to $0.6\ M_\odot / L_{\odot,3.6\mu\rm m}$. The mass-to-light ratio at 4.5 μm should be similar or even less than the mass-to-light ratio at 3.6 μm (Oh et al. 2008). This is in agreement with our results from the Jeans models of $0.56^{+0.22}_{-0.26}\ M_\odot / L_{\odot,4.5\,\mu\rm m}$. However, our best fit black hole mass is too low compared to direct measurements, and this might influence the outcome of Υ. We tested the magnitude of this by using the black hole mass of $4 \times 10^6\ M_\odot$ as input. Then Υ decreases to 0.35, which is still above our lower limit value. This test shows that our result of Υ is robust under local variations of the stellar populations, since the kinematic data covers a large enough region.

Our enclosed mass profile is shown in Fig. 2.17 using our best fit mass-to-light ratio Υ= $0.56^{+0.22}_{-0.26}\ M_\odot / L_{\odot,4.5\,\mu\rm m}$ for $0.3'' < r < 50'$. This plot contains the enclosed mass from both

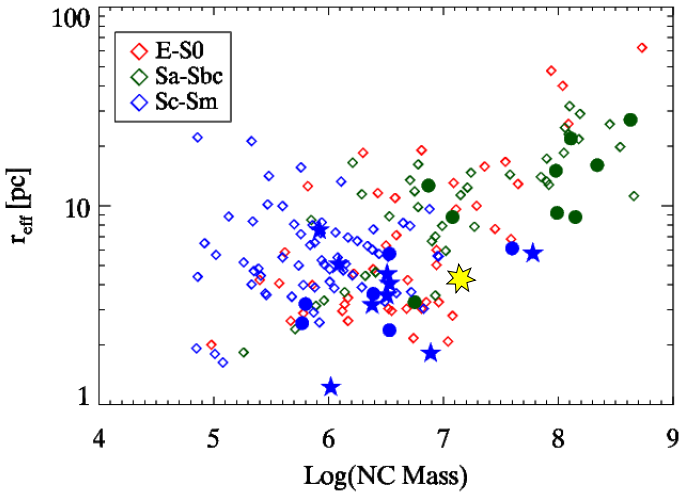

Figure 2.18: Nuclear cluster mass $M_{\rm NSC}$ − effective radius $r_{\rm eff}$ relation for nuclear star clusters, based on Seth et al. (2008a) with data from Walcher et al. (2005); Rossa et al. (2006) shown as filled symbols and Böker et al. (2002); Carollo et al. (1997, 1998, 2002); Côté et al. (2006) as open symbols. The yellow star is the result for the Milky Way nuclear star cluster within an effective radius of 4.2 pc (Schödel et al. 2014a).

the nuclear star cluster and the nuclear stellar disc, which dominates the mass at r ≳ 100 pc (40′). We also plot the results for the enclosed mass for various other studies, among those McGinn et al. (1989) and Lindqvist et al. (1992a) in Fig. 2.17. Those two studies assumed a Galactocentric distance of 8.5 kpc, while we assume 8.0 kpc. Further, they computed the mass by integrating the light enclosed in circles, and not ellipses, and assumed spherical symmetry. These are probably more important effects. The results of McGinn et al. (1989) for the enclosed mass tend to be higher at r < 30″, but we have good agreement with McGinn et al. (1989) at larger radii, and also with the results of Lindqvist et al. (1992a). One out of three of the values given by Trippe et al. (2008) is higher than our upper limit, while the other two data points agree with our results. The results of Oh et al. (2009) are in excellent agreement with our data inside 100″. At 28^{+28}_{-9}″ ($1.1^{+1.1}_{-0.3}$ pc), the mass of the stars equals the mass of the SMBH. Inside this radius the potential is dominated by the SMBH and therefore close to spherically symmetric. Merritt (2004) defines the radius of influence $r_{\rm infl}$ of a SMBH as the radius at which the enclosed mass in stars is twice the mass of the black hole. With this definition we obtain a mean radius $r_{\rm infl} = 60^{+54}_{-17}$″ ($2.3^{+2.1}_{-0.7}$ pc). This value is in agreement with the result of 3 pc found by Alexander (2005), based on the enclosed mass of Schödel et al. (2003).

Studies of Côté et al. (2006) and Forbes et al. (2008) showed that for nuclear star clusters the effective radii increase with the luminosity of the nuclear star cluster. This indicates also a correlation of the nuclear star cluster mass $M_{\rm NSC}$ to $r_{\rm eff}$. We plot this relation for a large number of nuclear star clusters compiled by Seth et al. (2008a) in Fig. 2.18; solid points

represent the most reliable mass estimates from Walcher et al. (2005) and Rossa et al. (2006). Other data points are from Böker et al. (2002); Carollo et al. (1997, 1998, 2002); Côté et al. (2006) and the mass estimate was derived purely photometrically. The yellow star denotes the mass of the Milky Way nuclear star cluster of $1.4 \times 10^7\,M_\odot$ within the effective radius. The $M_{\rm NSC} - r_{\rm eff}$ relation breaks down for low masses. The Milky Way nuclear star cluster is within the trends defined by other clusters, but is somewhat more compact than average.

2.6.4 Anisotropy

Schödel et al. (2009) found that the velocity dispersion of the late-type stars in the cluster is consistent with isotropy. This was confirmed by Do et al. (2013b) for the inner 0.5 pc of the Galaxy. We assumed different radial anisotropy profiles, but there is no clear trend about which profile fits best. However, the models favour tangential anisotropy, and if we impose constant anisotropy throughout the model, the best-fit value is $-0.3^{+0.3}_{-0.4}$, i.e. radial anisotropy is excluded. Also our analysis of λ_R suggests the Milky Way nuclear star cluster is anisotropic. Specifically, the cluster appears to be more flattened than expected based on the observed rotation.

2.6.5 Extreme velocities for individual stars

We extracted 1 375 spectra from bright stars with $K_S < 11.5$ mag from our unbinned data and fitted their velocities in Section 2.3.2. For three stars we obtained velocities higher than $250\,\mathrm{km{\cdot}s^{-1}}$, they are listed in Table 2.1. One is already known as IRS 9, and at a projected distance of 8″ from Sgr A* with $V = -340\,\mathrm{km{\cdot}s^{-1}}$. Its velocity was already measured by Zhu et al. (2008) to $-347.8\,\mathrm{km{\cdot}s^{-1}}$. The other stars are further out, at 80″ and 130″ distance, and have radial velocities of $292\,\mathrm{km{\cdot}s^{-1}}$ and $-266\,\mathrm{km{\cdot}s^{-1}}$. This corresponds to 3.5σ and 3.8σ in the velocity distribution of individual stars. These extreme velocities are even more surprising in their position as the local velocity dispersion around these stars is low. It is possible that these stars have been accelerated by the Hills mechanism. Hills (1988) predicted the existence of hypervelocity stars, which were ejected in a three-body encounter between the SMBH and a binary star system. Depending on the semi-major axis distance of the binary and the closest approach to the SMBH, stars can be accelerated to velocities of some $1\,000\,\mathrm{km{\cdot}s^{-1}}$. Since the stars detected by us have velocities of $-266\,\mathrm{km{\cdot}s^{-1}}$ and $292\,\mathrm{km{\cdot}s^{-1}}$, they would require a proper motion component of $\sim 960\,\mathrm{km{\cdot}s^{-1}}$ to reach a magnitude of the velocity vector of $\sim 1\,000\,\mathrm{km{\cdot}s^{-1}}$. Therefore we do not consider them as strong hypervelocity star candidates. Nevertheless, these stars could have been accelerated by the Hills mechanism.

2.7 Conclusions

We obtained an integral field like spectroscopic data set of the Milky Way nuclear star cluster. These data cover the central 11 arcmin^2 (60 pc^2), and six smaller fields at larger projected distances. Those go out to 8′ distance from Sgr A* along the Galactic Plane and cover

3.2 arcmin^2 in total. We set up a spectroscopic map with a pixel size of 2.″22 of the central field. Additionally we constructed a spectroscopic map that was cleaned of bright stars and foreground stars. Using these data cubes, we fitted the stellar CO absorption lines and computed velocity and velocity dispersion maps.

1. We found a misalignment of the photometric and kinematic position angles by ∼9° Galactic east of north. Further, we detected indications for a new kinematic substructure that is approximately aligned along the Galactic minor axis at ∼20″ (0.8 pc) distance from Sgr A*. Both observations indicate to different accretion events of the Milky Way nuclear star cluster. To confirm these findings with higher spatial resolution and a wider wavelength range we plan new observations with KMOS (VLT). If confirmed, the position angle offset and the substructure give important clues to the formation history of nuclear star clusters. They support the theory that infalling massive clusters play a role in the build-up of nuclear star clusters.

2. Axisymmetric Jeans models of the velocity maps underestimated the mass of the supermassive black hole in the Galactic centre. The reason for this can partially be explained by the lack of old stars in the central 0.5 pc. Therefore our measured velocity dispersion was biased to too low values. Another possibility is that the kinematic misalignment influences the outcome of the models. We cannot exclude a systematic bias in black hole mass measurements obtained using integrated light. Such a bias could mean that we underestimate black hole masses in some other galaxies as well. Therefore we plan to investigate this issue further using additional data in a follow-up paper.

3. We fitted a surface brightness profile of the Milky Way nuclear star cluster using NACO K_S-band data and *Spitzer* photometry at 4.5 μm. Our best-fit Jeans models resulted in a mass-to-light ratio $\Upsilon = 0.56^{+0.22}_{-0.26}\, M_\odot / L_{\odot,4.5\mu\mathrm{m}}$. From these results we computed a profile for the enclosed mass. At a distance of $r_{\mathrm{eff}} = 4.2$ pc from Sgr A* the cluster mass (without the black hole mass) is $(1.4^{+0.6}_{-0.7}) \times 10^7\ M_\odot$. Compared to nuclear star clusters of similar size the Milky Way nuclear star cluster is rather massive.

Acknowledgements

This research was supported by the DFG cluster of excellence Origin and Structure of the Universe (www.universe-cluster.de). This publication makes use of data products from the Two Micron All Sky Survey, which is a joint project of the University of Massachusetts and the Infrared Processing and Analysis Center/California Institute of Technology, funded by the National Aeronautics and Space Administration and the National Science Foundation. This research made use of the SIMBAD database (operated at CDS, Strasbourg, France). We would like to thank the ESO staff who helped us to prepare our observations and obtain the data. A special thanks to our Telescope operator J. Navarrete, who implemented all our non-standard observing techniques. A. F. also thanks Holger Baumgardt and Eric Emsellem for helpful discussions about the project. We thank Fabio Antonini for further investigations

of his simulations on our behalf and providing us additional information. C. J. W. acknowledges support through the Marie Curie Career Integration Grant 303912. We finally thank the anonymous referee for useful comments and suggestions.

Based on observations collected at the European Organisation for Astronomical Research in the Southern Hemisphere, Chile (289.B-5010(A)).

2.8 Appendix: Persistence removal

Persistence is a known problem of infrared detectors when observing bright sources. If the exposure time is too long and the source is overexposed, there can be ghost images of the source in a subsequently taken exposure of a faint source. The magnitude of the persistence effect decreases in time according to a power-law (Dressel 2012). To avoid persistence, one should either choose short exposure times or, alternatively, make a sequence of read-outs afterwards, to flush the detector's memory of the bright source. We took acquisition images right before the object spectra, which lead to persistence in the 2D spectra. Also our 2D sky spectra are affected as we took three dithered images on source before the sky offsets to verify the position on the sky after the drift, and two dithered images on sky that also contain a few stars.

However, we developed a way to remove the persistence signature completely in our sky frames and to some extent also in the object spectra. We used the images that cause the persistence and the corresponding 2D spectra that are affected by the persistence. Removing persistence from the 2D sky spectra is rather straight forward: For every 2D sky spectrum $S_{\mathrm{raw,sky}}$ we computed the median of each column along the dispersion axis and subtracted it from each pixel in the column, and did the same with the median along the spatial axis to get a 2D sky spectrum without any lines or stars $S_{\mathrm{med,sky}}$. The only features left in the median subtracted 2D sky spectrum are from the persistence. Then one can simply compute a corrected 2D sky spectrum $S_{\mathrm{cor,sky}}$

$$S_{\mathrm{cor,sky}} = S_{\mathrm{raw,sky}} - S_{\mathrm{med,sky}} + \mathrm{mean}(S_{\mathrm{med,sky}}). \tag{2.4}$$

The clean 2D sky spectra were combined to 2D Mastersky spectra using IRAF. We also produced noise files for each sky file that contain the information about the persistence correction.

This simple approach is not possible for the 2D object spectra, as there are many stars with strong absorption lines and also an H_2 gas emission line. In contrast to the 2D sky spectra, subtracting a median leaves other strong features apart from the persistence residuals. Therefore we decided to model the persistence and subtracted the model from the 2D object spectra. To determine the persistence model parameters we used the 2D sky spectra before we applied the aforementioned correction on them.

Saturated pixels have negative counts in our images and leave persistence features in the 2D spectra taken afterwards. Persistence is also a problem if the counts of a bright source at a given pixel of the detector are above a certain threshold. First, one needs to determine

the value of this threshold. Therefore we considered only counts above a trial threshold and made a persistence mask M, where pixels with negative counts in the image as well as counts above the threshold were set to one and all other pixels were set to zero. As the raw 2D sky frames are affected by persistence coming from three images on source and two images on sky, taken ~2–3 minutes later, we made two masks, one for the images on source ($M_{\rm source}$) and one for the sky images ($M_{\rm sky}$). Then we used MPFIT2DFUN.PRO (Markwardt 2009) to fit the amplitudes of the persistence, $K_{\rm source}$ and $K_{\rm sky}$, and a full-width-half-maximum FWHM for a Gaussian smoothing filter $G_{\rm FWHM}$ of the masks. The residual spectrum R is

$$R = S_{\rm med} - G_{\rm FWHM} * (K_{\rm source} \times M_{\rm source} + K_{\rm sky} \times M_{\rm sky}), \tag{2.5}$$

where the symbol "$*$" denotes convolution. We tried different values of the mask threshold, and we found a minimum of the standard deviation of the residual spectrum R at a threshold of 33,500 counts. Therefore we defined 33,500 counts as our threshold for further corrections of images taken with an exposure time of $20s$. For the images with exposure time $t = 5s$, we have a lower threshold of 24,000 counts, found by the same method.

The next step is to fit $K_{\rm source}$, $K_{\rm sky}$, and FWHM with the chosen threshold value of the mask for every median subtracted 2D sky spectrum $S_{\rm med,sky}$. The persistence signal decreases in time, therefore $K_{\rm source}$ and $K_{\rm sky}$ decrease from the first to the fifth 2D sky spectrum in a sequence. We fitted the decrease of K with the power law

$$K(t) = A \times t^{-\gamma}, \tag{2.6}$$

where the parameter A is the amplitude and γ is a scale factor. We did this for $K_{\rm source}$ and $K_{\rm sky}$ separately and together, but our later analysis shows that we obtain better results when we use the result of fitting $K_{\rm source}(t)$ alone. The parameters we used are $A = (6\,900 \pm 1\,700)$ and $\gamma = (0.98 \pm 0.04)$. The uncertainties are the formal 1-σ errors of the fit. With this knowledge we can subtract the persistence from the 2D object spectra with the equation

$$S_{\rm cor,object} = S_{\rm raw,object} - (G_{\rm FWHM} * M_{\rm acqu}) \times A \times t^{-\gamma}. \tag{2.7}$$

The images causing persistence in the 2D object spectra are acquisition images. As we made acquisition offsets, we subtracted persistence caused by the acquisition image itself and from a shifted acquisition image. We have only the acquisition image itself as file, but we can identify the shift in pixels from the persistence in the 2D spectra, and we can fit the shift of the acquisition offset together with an attenuation factor α. This factor α is necessary as the offset was performed before the acquisition image was taken, and therefore the persistence signal is weaker. In this case the corrected 2D object spectra $S_{\rm cor,object}$ are

$$\begin{aligned} S_{\rm cor,object} = S_{\rm raw,object} &- (G_{\rm FWHM} * M_{\rm acqu}) \times A \times t^{-\gamma} \\ &- \alpha \times (G_{\rm FWHM} * M_{\rm acqu,shifted}) \times A \times t^{-\gamma}. \end{aligned} \tag{2.8}$$

With these procedures it is possible to remove the persistence structures completely from the 2D sky frames and to subtract them from the 2D object spectra partially, but some residuals still remain. In some cases we made more than one acquisition offset, and furthermore it

is difficult to model the shape of the persistence, which was slightly elliptical due to the drift during the acquisition. The shape also changes depending on the area on the detector and seeing conditions. To account for uncertainties in the persistence subtraction, we made noise files that were used for the further analysis of the spectra.

To check the influence of the persistence after the correction on our results we compared two 2D spectra that cover almost the same region of the Milky Way nuclear star cluster. One 2D spectrum was not affected by the persistence, since it was the 20th exposures taken after the acquisition image. The other 2D spectrum was taken shortly after the acquisition image and was affected by persistence. We extracted several 1D spectra by summing between 45 and 100 rows of the 2D spectra. Then we fitted the CO absorption lines with pPXF. The signal-to-noise ratio (S/N) of the spectra taken from the file with persistence, but after our correction, is lower by ∼27 per cent compared to the S/N of spectra from the file with no persistence. But as the effect of persistence decreases in time, not all of our data are as much affected. We estimate that in ∼70 per cent of our spectra the decrease in S/N due to the persistence is less than 20 per cent.

2.9 Appendix: H_2 gas emission kinematics

We fitted the 1-0 Q(1) 2.4066 μm transition of H_2 to make a comparison with previous studies (e.g. Gatley et al. 1986; Yusef-Zadeh et al. 2001; Lee et al. 2008). The excellent agreement of our flux and kinematic maps with these studies shows that our data can reproduce previous results without strong biases. Figure 2.19 illustrates the results of the fitting for flux, velocity and velocity dispersion. Regions where the flux was too low and confusion with sky line residuals might be possible are not displayed. In the H_2 velocity map we can identify the northeastern and southwestern lobe of the circumnuclear disc (see Fig. 1 of Amo-Baladrón et al. (2011) for an illustration of the central 12 pc).

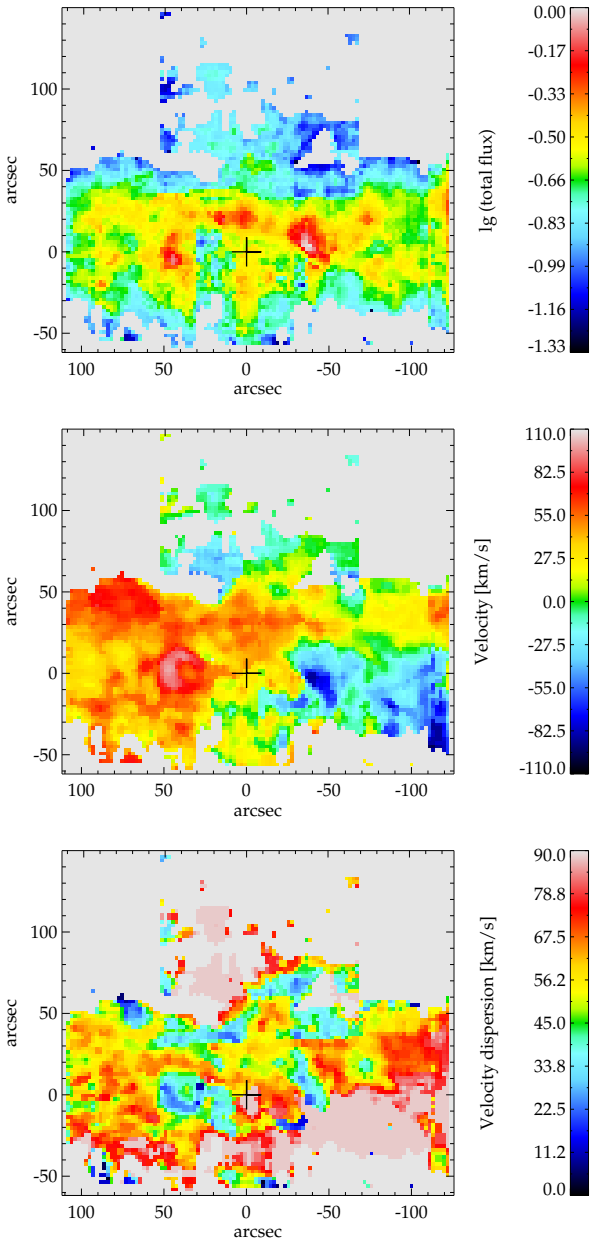

Figure 2.19: Results of the single Gaussian fit to the H_2 gas emission line. Upper panel: flux in logarithmic scaling and with respect to the maximum flux. Middle panel: velocity in $km{\cdot}s^{-1}$. Lower panel: velocity dispersion in $km{\cdot}s^{-1}$, corrected for the instrumental dispersion ($\sigma_{instr} \approx 27\,km{\cdot}s^{-1}$). The coordinates are centred on Sgr A* and along the Galactic plane with a position angle of 31.°40. The cross marks the position of Sgr A*.